

## Extended classification of the buoyancy-driven flows induced by a neutralization reaction in miscible fluids. Part 2. Theoretical study

D.A. Bratsun<sup>1,†</sup>, A.I. Mizev<sup>1,2</sup> and E.A. Mosheva<sup>1,2</sup>

<sup>1</sup>Perm National Research Polytechnic University, Perm 614990, Russia

<sup>2</sup>Institute of Continuous Media Mechanics, Russian Academy of Science, Perm 614013, Russia

(Received 3 June 2020; revised 24 January 2021; accepted 3 March 2021)

The buoyancy-driven chemoconvection induced by a neutralization reaction is theoretically studied for a system consisting of nitric acid and sodium hydroxide aqueous solutions placed in a vertically oriented Hele-Shaw cell. This pair of reactants is a representative case of reacting miscible acid–base systems investigated experimentally in Part 1 of this work (Mizev *et al.*, *J. Fluid Mech.*, vol. 916, 2021, A22). We showed that the list of the possible instabilities in this system is much richer than previously thought. A new scenario for pattern formation depends on a single parameter denoted by  $K_\rho$ , the reaction-induced buoyancy number defined in Part 1. In this paper, the theoretical analysis complementing the experimental observations provides the conceptual insights required for a full understanding of the mechanisms of the observed phenomena. The mathematical model we develop consists of a system of reaction–diffusion–advection equations governing the evolution of concentrations coupled to the Navier–Stokes equation. The system dynamics is examined through transient linear stability analysis and numerical simulation. If  $K_\rho > 1$ , then a statically stable potential well appears adjacent to the reaction front. As a result, a Rayleigh–Bénard-like cellular pattern can arise in this depleted density region. If  $K_\rho \leq 1$ , then a potential well collapses, and a shock-wave-like structure with an almost planar front occurs. This wave propagates fast compared with the diffusion time and acts as a turbulent bore separating immobile fluid and an area of intense convective mixing. Finally, we determine the place of the above instabilities in an extended classification of known instability types.

**Key words:** buoyancy-driven instability, Hele-Shaw flows

† Email address for correspondence: [dabracun@pstu.ru](mailto:dabracun@pstu.ru)

## 1. Introduction

In recent years, the interaction between reaction–diffusion phenomena and convective instabilities has attracted increasing interest both from the fundamental point of view and numerous applications. As shown, the reaction–diffusion processes and fluid motion can establish positive feedback. On the one hand, the chemically induced changes of fluid properties, such as concentration, density, viscosity or surface tension, may result in instabilities, which exhibit a large variety of convective patterns. On the other hand, convective flows can significantly change the distribution of reactants in the medium, setting new scenarios for the reaction.

An exothermic neutralization reaction occurring in a two-layer miscible system has been actively studied in recent years because of a comparatively simple, but nonlinear, kinetics. If two miscible solutions are brought into contact in zero gravity, then the reaction can form a front. The papers (Gálfi & Rácz 1988; Koza & Taitelbaum 1996) considered the properties of an  $A + B \rightarrow C$  chemical front in the framework of a reaction–diffusion approach. If the reaction occurs in a two-layer miscible system under gravity, it may result in various buoyancy-driven instabilities, which were intensively studied both experimentally and theoretically in the last decade (Zalts *et al.* 2008; Almarcha *et al.* 2010; Hejazi & Azaiez 2012; Tsuji & Müller 2012; Lemaigre *et al.* 2013; Kim 2014, 2019). For the most complete recent review on this topic, see De Wit (2020).

In the non-reactive case, pattern formation in the form of irregular plumes and fingers is observed when the upper layer is denser than the lower one. This stratification is unstable under gravity via a Rayleigh–Taylor (hereinafter abbreviated to RT) instability. It is important to note that the density fingering develops similarly above and below the initial contact surface since the underlying density gradient is symmetric (Fernandez *et al.* 2002; Trevelyan, Almarcha & De Wit 2011; Carballido-Landeira *et al.* 2013). By contrast, the RT fingering triggered by the reaction can develop asymmetric patterns (Zalts *et al.* 2008; Almarcha *et al.* 2010; Lemaigre *et al.* 2013). The reason is that the downward-moving denser reactant dissolved in the upper layer is consumed by the reaction and replaced by the salt of lower density (De Wit 2020).

Another important engine breaking the equilibrium in a liquid is the difference between the diffusion rates of species resulting in either a double-diffusive (DD) instability (Stern 1960) or diffusive-layer convection (DLC) (Stern & Turner 1969). If the initial stratification is statically stable, the DD instability occurs if the solute dissolved in the lower layer diffuses faster, while the DLC mode occurs if the opposite is true. And again, in the absence of reaction, the DD convection is symmetric (Fernandez *et al.* 2002; Trevelyan *et al.* 2011), but the reaction produces asymmetric patterns (Lemaigre *et al.* 2013; De Wit 2020). Finally, the paper (Trevelyan, Almarcha & De Wit 2015) classified all possible types of buoyancy-driven instabilities that occur in two-layer miscible systems. Thus, the result of all these studies is the conclusion that a neutralization reaction does not give rise to new types of instabilities, but rather changes the features of previously well-known instability mechanisms (RT, DD and DLC).

In this review, it makes sense to also mention several papers devoted to immiscible systems studied under gravity. The statically unstable density profiles can generate spontaneous convective flows near the liquid–liquid interface. Such buoyancy-related patterns induced by chemically driven unfavourable density gradients have received increasing attention over recent decades (Avnir & Kagan 1984; Bees *et al.* 2001). Convective phenomena related to heat and solutal buoyancy effects due to an exothermic  $A + B \rightarrow C$  neutralization reaction close to a liquid–liquid interface have been studied experimentally by Eckert & Grahn (1999) and Eckert, Acker & Shi (2004). Their first

experimental system consisted of an organic solution containing a carboxylic acid put in contact in a Hele-Shaw cell with an aqueous solution in which sodium hydroxide was dissolved. Dynamics and patterns in the form of irregular plumes and fingers are observed (Eckert & Grahn 1999). When propionic acid was dissolved in the upper layer and NaOH was replaced by an organic base, the impressive regular fingered structure in the form of long self-growing cells with one side keeping contact with the interface and the other side propagating downwards out of the interface was observed in the same system (Eckert *et al.* 2004). Those observations may be relevant to the effects discussed in this paper.

We have recently demonstrated in Bratsun *et al.* (2015, 2017) that the interaction of the buoyancy-driven flow and the neutralization reaction can lead to much more radical scenarios of the pattern formation. The format of the short communications of those publications made it impossible to describe the obtained results consistently. The goal of this work, which is divided into Part 1 (experiment) and Part 2 (theory), is to provide a comprehensive experimental and theoretical study on recently revealed pattern formations and to find their place in the general classification of instabilities.

In Part 1 of this work (Mizev, Mosheva & Bratsun 2021), we have introduced a reaction-induced buoyancy number  $K_\rho$  defined as the ratio of the density of the reaction zone to that of the upper layer. As was shown experimentally in Part 1, the pattern formation in the system depends on the value of this non-dimensional parameter. If  $K_\rho > 1$ , then the process is governed mainly by diffusion, which results in the development of relatively weak convective motion caused by the differential-diffusion effect. Besides the irregular density fingering, reported earlier in numerous studies, we found a new type of instability, a concentration-dependent diffusion (CDD) convection, which is characterized by the formation of a regular cellular convective pattern. If  $K_\rho \leq 1$ , then the entire reaction zone becomes unstable, giving rise to the vigorous convection in the form of the shock-wave-like (SW) structure. It forces the reaction front to move down fast so that it takes just a few minutes for reactants to burn out. This effect has been revealed and carefully studied in different pairs of reactants, which provides proof of the versatility of the instability mechanisms. In Part 2, the theoretical analysis complementing the experimental observations presented in Part 1 provides the conceptual insights required for a full understanding of the mechanisms of the observed phenomena.

## 2. Problem formulation

### 2.1. Reaction kinetics

We study a two-layer system consisting of miscible solutions initially separated by a horizontal contact plane (figure 1). The upper layer of the system is always of lower density than the lower one, which allows us to exclude the development of a global RT instability from the very beginning of the study. We assume that nitric acid  $A$  (it can initially be either in the upper or lower layer) diffuses to react with sodium hydroxide  $B$  to form their salt  $C$  under the production of water. This process is accompanied by significant heat release  $Q$ . The standard enthalpy of the reaction is  $57 \text{ kJ mol}^{-1}$ . Such a neutralization reaction can be described by the simplified equation



with the reaction rate characterized by the constant  $K$ . Thus, a second-order exothermic neutralization reaction defined by (2.1) has a comparatively simple, albeit nonlinear, kinetics.

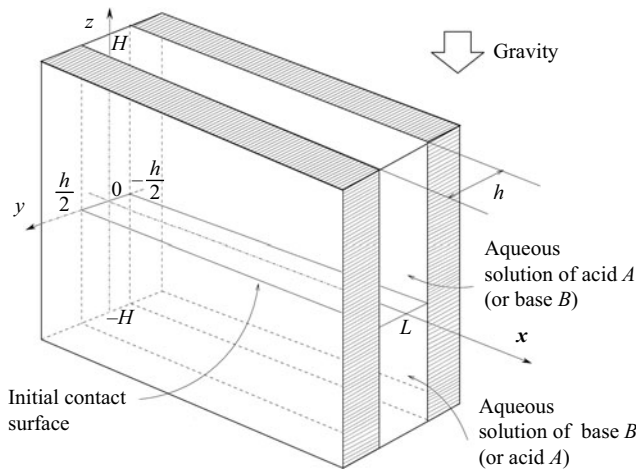


Figure 1. Geometrical configuration of the two-layer miscible system and coordinate axes.

### 2.2. Hele-Shaw flow approximation

The Hele-Shaw cell, since its description by Hele Shaw (1898), has proven to be a useful instrument to study quasi-two-dimensional flows. These flows develop between two parallel flat plates separated by an infinitesimally small gap. As is well known, Hele Shaw's theory for single-phase flow results in the depth-averaged equations for pressure and two-dimensional velocity fields. In the simplest case, the Hele-Shaw approximation reduces the equation of motion to Darcy's law formulated initially for the fluid filtration through a porous medium. In this limit, the flow in the Hele-Shaw cell is completely analogous to the fluid filtration through a porous medium. The majority of works, which we cited above, have used the Darcy model to describe the phenomena in the system under consideration (Almarcha *et al.* 2010; Hejazi & Azaiez 2012; Tsuji & Müller 2012; Lemaigre *et al.* 2013; Kim 2014; Trevelyan *et al.* 2015). It should be noted that the Darcy equation for the description of fluid flow in porous media is valid under the condition that the mean velocity varies slowly in space (Zeng, Yortsos & Salin 2003). In many cases, however, this condition is not met. For example, this may be due to a sharp change in fluid properties, as in the context of the RT problem Martin, Rakotomalala & Salin (2002), or in viscous fingering (Martin *et al.* 2011), or due to the presence of the interface in the immiscible system, which requires the correct formulation of the boundary conditions for the velocity (Bratsun & De Wit 2004). The simplest way to correct this inadequacy in the model is to add the term suggested by Brinkman (1947). A more complicated correction implies taking into account the inertial term in a special form in the equation of motion, as was suggested by Ruyer-Quil (2001) and Martin *et al.* (2002).

The system we consider consists of two vertical solid plates placed parallel to each other with a small distance between them. Let  $x, z$  be the directions parallel to the flat plates, and  $y$  the perpendicular direction, with  $h$  the gap between the plates at  $y = \pm h/2$  (see figure 1). For the sake of clarity, suppose that the  $z$ -axis is anti-directed to gravity. The resulting closed cavity is defined by  $0 \leq x \leq L$  and  $-H \leq z \leq H$ .

We start with a three-dimensional Navier–Stokes equation, coupled with a continuity equation, implying that the fluid is incompressible

$$\nabla \cdot \mathbf{u} = 0, \tag{2.2}$$

$$\hat{\rho} \left( \frac{\partial \mathbf{u}}{\partial t} + \mathbf{u} \cdot \nabla \mathbf{u} \right) = -\nabla p + \eta \nabla^2 \mathbf{u} + \hat{\rho} \mathbf{g}. \quad (2.3)$$

Here,  $\mathbf{u} : (u_x, u_y, u_z)$  is the velocity,  $\hat{\rho}$  is the solution density and  $p$  is the pressure;  $\eta$  and  $\mathbf{g}$  stand for the dynamic viscosity and the acceleration vector due to gravity, respectively. Under the assumption that the fluid adheres to the solid walls, the boundary conditions for the velocity at the solid plates are

$$y = \pm \frac{h}{2} : \quad \mathbf{u} = 0. \quad (2.4a,b)$$

We further assume that the gap width  $h$  is small enough so that the fluid flow may be considered as quasi-two-dimensional, i.e. a Hele-Shaw approximation is applicable. Taking into account the boundary condition (2.4a,b), the velocity can be approximated by the following functions:

$$\left. \begin{aligned} u_x(x, y, z) &= \frac{3}{2} \left( 1 - \frac{4y^2}{h^2} \right) U(x, z), \\ u_y(x, y, z) &= 0, \\ u_z(x, y, z) &= \frac{3}{2} \left( 1 - \frac{4y^2}{h^2} \right) V(x, z), \end{aligned} \right\} \quad (2.5)$$

where  $\mathbf{v} : (U, V)$  is the two-component velocity field obtained after averaging the velocity  $\mathbf{u}$  across the gap.

The approximations (2.5) should then be substituted into the Navier–Stokes equation (2.3) and averaged across the gap

$$\langle \dots \rangle = \frac{1}{h} \int_{-h/2}^{h/2} \dots dy. \quad (2.6)$$

As a result, we obtain the motion equation written in the Hele-Shaw approximation

$$\rho_0 \left( \frac{\partial \mathbf{v}}{\partial t} + \frac{6}{5} \mathbf{v} \cdot \nabla \mathbf{v} \right) = -\nabla p + \eta \Delta \mathbf{v} - \frac{12\eta}{h^2} \mathbf{v} + \langle \rho \rangle \mathbf{g}, \quad (2.7)$$

where  $\rho_0$  is the density of the solvent and  $\langle \rho \rangle$  is the average medium density, which will be determined below. In addition to the correction factor 6/5 (Ruyer-Quil 2001), (2.7) differs from the standard Navier–Stokes equation by the term proportional to the velocity. One can interpret this term as the average friction force due to the presence of the plates, and it is analogous to Darcy’s law for the porous medium.

Let us estimate whether it is necessary to use the Hele-Shaw approximation in the form (2.7), which includes the Brinkman term and the inertial term, in this problem. We define the characteristic size of the chemoconvective structure as  $H$ , which can be estimated as  $\sqrt{\tau_R D_{a0}}$ , where  $\tau_R = 1/KA_0$  stands for the characteristic reaction time and  $D_{a0}$  is the table value of the diffusion coefficient of acid. Then we scale the equation (2.7) choosing the following characteristic units: for time  $\tau_R$ , for length  $H$ , for velocity  $H/\tau_R$ , for pressure

$12\rho_0\nu D_{a0}/h^2$  and obtain

$$\frac{\varepsilon}{Sc} \left( \frac{\partial \mathbf{v}}{\partial t} + \frac{6}{5} \mathbf{v} \cdot \nabla \mathbf{v} \right) = -\nabla p + \varepsilon \Delta \mathbf{v} - \mathbf{v} + \varepsilon Sc Ga \frac{\langle \rho \rangle}{\rho_0} \mathbf{z}, \quad (2.8)$$

where  $Sc$  is the Schmidt number,  $Ga$  is the Galileo number and

$$\varepsilon = \frac{h^2}{12H^2} = \frac{h^2 \sqrt{KA_0}}{12\sqrt{D_{a0}}} \quad (2.9)$$

stands for the parameter determining the relative contribution of the Brinkman term to the motion equation.

In addition, we can evaluate the applicability of the Hele-Shaw approximation by reasoning in terms of the convective instability itself, regardless of the characteristic size of the cavity, which largely imposes its scale on physical processes. In our problem, there are two fundamental types of instabilities: RT convection and diffusive instability. Let us estimate the characteristic wavelength of each instability expressed in terms of diffusion, viscosity and buoyancy. An estimate of the characteristic length of diffusive types of instabilities can be obtained using the formula derived by Stern (1960). Stern considered doubly stratified water: warm and salty above cold and fresh, that is typical for the ocean stratification, and was the first to explain the mechanism of the onset of double-diffusion instability. Since, in our work, the role of heat is played by a rapidly diffusing acid, we must replace the characteristics of the thermal field in the Stern formula with the characteristics of the acid concentration field. Then, we obtain the estimate for an aqueous solution of nitric acid

$$L_{DD} = \pi \left( \frac{4\nu D_{a0}}{g\beta_a |G_a|} \right)^{1/4} \approx 0.7 \text{ mm}, \quad (2.10)$$

where  $\beta_a$  is the acid expansion coefficient and  $G_a$  is the characteristic vertical gradient of acid concentration in the domain where the instability occurs. To obtain (2.10), we have used the data presented in table 1 of Part 1 (Mizev *et al.* 2021).

To estimate the characteristic size of the RT convection at the very beginning of the evolution, we can use the formula suggested by Martin *et al.* (2002). The authors have introduced the characteristic length  $L_{RT}$  for the RT instability developing in miscible systems. For our case, we get the following estimate:

$$L_{RT} = \left( \frac{2\rho_0\nu D_{a0}}{g\Delta\rho} \right)^{1/3} \approx 0.1 \text{ mm}, \quad (2.11)$$

where  $\Delta\rho$  stands for the characteristic density difference giving rise to the RT instability.

We can learn from the estimates (2.10) and (2.11) that the characteristic instability length is either of the same order of magnitude as the Hele-Shaw cell gap ( $h = 1 \text{ mm}$ ) used in the experiment or even smaller. This serves as another justification for using the Navier–Stokes–Darcy model equation (2.7) instead of the simple Darcy model. What is important is that the use of the averaged two-dimensional Navier–Stokes–Darcy equation (2.7) allows us to unify all limiting cases. The Darcy model for the Hele-Shaw cell description is valid when the cell gap is small compared to this characteristic reaction–diffusion length ( $\varepsilon \ll 1$ ), whereas the case of fully three-dimensional flows governed by the Navier–Stokes equation is obtained in the opposite limit ( $\varepsilon \gg 1$ ). The use of the equation (2.7) allows us to recover these two limits and to give a good approximation in the intermediate range of cell thicknesses (Ruyer-Quil 2001; Martin *et al.* 2002).



We can learn from the experimental observations (Mizev *et al.* 2021) that, at the very beginning of evolution (at  $t < 200$  s in dimensionless units), the characteristic size of the structures can be small enough and the diffusion represented by the Brinkman term in (2.7) can play an important role in the system dynamics. At later stages of evolution ( $t > 200$  s), Darcy's law can be used to model flows. In fact, the situation is ambiguous, since chemoconvective cells form for a rather long time. In the case of the SW mode, the processes are much faster, but the characteristic size of convective structures is larger. Summarizing all of this, we can state that the use of the full three-dimensional Navier–Stokes equations in this problem is redundant, but the use of the Brinkman term is desirable.

All other physical fields should be averaged in the same style as the velocity.

### 2.3. Boussinesq approximation

The Boussinesq approximation is commonly applied in convection theory to describe buoyancy-driven flows. This approximation embodies two essential ideas. First, any fluctuations in density that occur with the onset of fluid motion are produced mainly by either thermal effects (in the case of thermally induced buoyancy) or by concentration effects (in the case of solutally induced buoyancy) rather than by pressure effects. The second idea is that all variations in fluid properties, except density, may be neglected. Furthermore, this approximation ignores density differences except where they appear in the terms responsible for the convective buoyancy force. The Boussinesq approach is justified for the problems in which ‘weak’ convection exists in the cavity on the laboratory scale, and the density variations caused by thermal or concentration expansion are relatively small.

In fact, we have already implicitly used the Boussinesq approach when we replaced the density function  $\rho$  on the left side of the motion equation (2.7) with a constant value  $\rho_0$  of the solvent density. To complete the work, one needs to expand the density  $\langle \rho \rangle$  on the right-hand side of (2.7) as a power series of temperature and concentrations, retaining only linear terms

$$\langle \rho \rangle = \rho_0 + \rho = \rho_0(1 - \beta T + \beta_a A + \beta_b B + \beta_c C), \quad (2.12)$$

where  $\beta$  and  $\beta_i$  are the thermal and solutal expansion coefficients, respectively. In (2.12), we take into account the fact that all the dissolved substances are heavier than water. Let us evaluate the contribution of thermal and solutal effects to the buoyancy force by composing the ratio of the first two terms of the first order in the expansion (2.12)

$$\frac{\beta \Theta^*}{\beta_a A^*} = Le \frac{\beta |Q| D_{a0}}{\beta_a \kappa} \approx 0.08, \quad (2.13)$$

where  $D_{a0}$  is the table value of the diffusion coefficient of acid,  $\kappa$  is the thermal conductivity of solvent and  $\Theta^*$  and  $A^*$  stand for the characteristic values of the temperature and acid concentration, respectively;  $Le$  stands for the Lewis number defined as the ratio of thermal diffusivity to mass diffusivity. To get an estimate (2.13), we have used data for water and nitric acid:  $Le = 42$ ,  $\beta = 0.207 \times 10^{-3} \text{ K}^{-1}$ ,  $\beta_a = 3.34 \times 10^{-2} \text{ l mol}^{-1}$ ,  $D_{a0} = 3.15 \times 10^{-5} \text{ cm}^2 \text{ s}^{-1}$ ,  $\kappa = 0.6 \text{ J s}^{-1} \text{ m}^{-1} \text{ K}^{-1}$ .

In addition to the evaluation (2.13), one can notice that the thick walls of the experimental Hele–Shaw cell are made from glass, which transmits significant heat because the thermal conductivity coefficients of water and glass are nearly the same. In comparison with the concentration effects, the thermal effects can be controlled to a

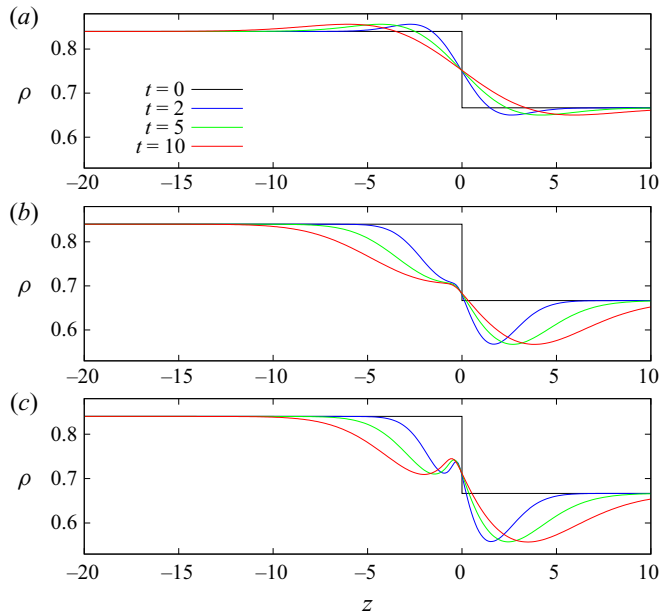


Figure 2. Instantaneous density profiles  $\rho^0(z, t)$  calculated for successive times in the case of pure diffusion (a), reaction–diffusion without the CDD effect (b) and reaction–diffusion influenced by the CDD effect (c). The position of the initial contact surface of the solutions is determined by the line  $z = 0$ . The initial concentrations are  $\gamma_a = 0.667$ ,  $\gamma_b = 0.7$ .

greater extent during the experiment. Thermally insulated walls enhance the role of heat, while perfectly conductive walls make the heat effect negligible.

Finally, one can learn from (2.13) that the thermally induced buoyancy is an order of magnitude weaker than the buoyancy force caused by the solute effect. For this reason, in what follows, we consider the problem as isothermal.

#### 2.4. Governing equations

As follows from the experimental observations presented in Part 1 of this work (Mizev *et al.* 2021), the processes that occur during the neutralization of a strong acid with alkali metal hydroxides are very similar. Therefore, we present the theoretical study for one characteristic pair of reactants: nitric acid and sodium hydroxide. So, let two miscible fluids fill the Hele–Shaw cell with a gap depth  $h$ , and let them be spatially separated at the very beginning by a contact surface  $z = 0$ . The upper (or lower) layer is an aqueous solution of  $\text{HNO}_3$ , and the lower (or upper) layer is an aqueous solution of  $\text{NaOH}$  (figure 2). The initial values of reactant concentrations are  $A_0$  and  $B_0$ . These two parameters are key to the problem since they are the only ones we can easily tune in the experiments with a fixed pair of reactants. In all cases considered below, the initial concentrations of reactants are selected so that the stratification of the system at the very beginning is statically stable. Thus, we exclude the occurrence of the RT instability.

We use  $h$  as the measurement unit for length and  $h^2/D_{a0}$  for time,  $D_{a0}/h$  for velocity,  $\rho_0\nu D_{a0}/h^2$  for pressure and  $A_{lim}$  for concentration, where  $A_{lim}$  is the maximum concentration at which the linear law of CDD is observed for nitric acid. The incompressibility constraint (2.2) can be satisfied automatically by defining a



streamfunction  $\Psi$  such that

$$U = -\frac{\partial \Psi}{\partial z}, \quad V = \frac{\partial \Psi}{\partial x}. \quad (2.14a,b)$$

In what follows, we use the vorticity–streamfunction formulation of the governing equations. Thus, the set of reaction–diffusion–advection equations written in the Boussinesq and Hele–Shaw approximations is as follows:

$$\Phi = -\nabla^2 \Psi, \quad (2.15)$$

$$\frac{1}{Sc} \left( \frac{\partial \Phi}{\partial t} + \frac{6}{5} \frac{\partial \Psi}{\partial z} \frac{\partial \Phi}{\partial x} - \frac{6}{5} \frac{\partial \Psi}{\partial x} \frac{\partial \Phi}{\partial z} \right) = \nabla^2 \Phi - 12\Phi - R_a \frac{\partial A}{\partial x} - R_b \frac{\partial B}{\partial x} - R_c \frac{\partial C}{\partial x}, \quad (2.16)$$

$$\frac{\partial A}{\partial t} + \frac{\partial \Psi}{\partial z} \frac{\partial A}{\partial x} - \frac{\partial \Psi}{\partial x} \frac{\partial A}{\partial z} = \nabla(D_a \nabla A) - DaAB, \quad (2.17)$$

$$\frac{\partial B}{\partial t} + \frac{\partial \Psi}{\partial z} \frac{\partial B}{\partial x} - \frac{\partial \Psi}{\partial x} \frac{\partial B}{\partial z} = \nabla(D_b \nabla B) - DaAB, \quad (2.18)$$

$$\frac{\partial C}{\partial t} + \frac{\partial \Psi}{\partial z} \frac{\partial C}{\partial x} - \frac{\partial \Psi}{\partial x} \frac{\partial C}{\partial z} = \nabla(D_c \nabla C) + DaAB, \quad (2.19)$$

where (2.15) is the definition of the vorticity  $\Phi$ . The diffusion terms in (2.17)–(2.19) have been written in the most general form taking into account the CDD effect (Crank 1975).

Equations (2.15)–(2.19) should be supplemented by the boundary conditions

$$x = 0, L: \quad \Psi = 0, \quad \frac{\partial \Psi}{\partial x} = 0, \quad \frac{\partial A}{\partial x} = 0, \quad \frac{\partial B}{\partial x} = 0, \quad \frac{\partial C}{\partial x} = 0, \quad (2.20a,b)$$

$$z = \pm L: \quad \Psi = 0, \quad \frac{\partial \Psi}{\partial z} = 0, \quad \frac{\partial A}{\partial z} = 0, \quad \frac{\partial B}{\partial z} = 0, \quad \frac{\partial C}{\partial z} = 0. \quad (2.21a,b)$$

If the acid solution is on the top, the initial conditions at  $t = 0$  are written as

$$z \leq 0: \quad \Psi = 0, \quad A = 0, \quad B = \gamma_b, \quad (2.22a,b)$$

$$z > 0: \quad \Psi = 0, \quad A = \gamma_a, \quad B = 0, \quad (2.23a,b)$$

where  $\gamma_a$  and  $\gamma_b$  stand for

$$\gamma_a = \frac{A_0}{A_{lim}}, \quad \gamma_b = \frac{B_0}{A_{lim}}, \quad (2.24a,b)$$

respectively.

If the base solution is on the top, the initial conditions are

$$z \leq 0: \quad \Psi = 0, \quad A = \gamma_a, \quad B = 0, \quad (2.25a,b)$$

$$z > 0: \quad \Psi = 0, \quad A = 0, \quad B = \gamma_b. \quad (2.26a,b)$$

The set of equations (2.15)–(2.19) has two dimensionless parameters

$$Sc = \frac{\nu}{D_{a0}}, \quad Da = \frac{KA_{lim}h^2}{D_{a0}}, \quad (2.27a,b)$$

the Schmidt number and the Damköhler number, respectively. These two numbers are the ratio of either the viscous diffusion rate or reaction rate to the mass diffusion rate, respectively. The evaluation of the Schmidt number for nitric acid gives the value

$Sc = 317$ . As for the Damköhler number, in this paper, we accept a comparatively high value, which makes the reaction frontal:  $Da = 10^3$ . Note that the above parameters (2.27a,b) are determined by the reaction kinetics, and they cannot be tuned in the experiments with a particular pair of reactants.

In addition, the set of Rayleigh numbers appears in (2.16)

$$R_a = \frac{g\beta_a A_{lim} h^3}{\nu D_{a0}}, \quad R_b = \frac{g\beta_b A_{lim} h^3}{\nu D_{a0}}, \quad R_c = \frac{g\beta_c A_{lim} h^3}{\nu D_{a0}}, \quad (2.28a-c)$$

characterizing the contribution of each water dissolved substance to density variations. The values of the parameters (2.28a-c) can also be estimated with the table values:  $R_a = 3.18 \times 10^5$ ,  $R_b = 3.82 \times 10^5$ ,  $R_c = 5.1 \times 10^5$ .

In what follows, it is convenient to define a variable based on the expansion (2.12), which makes sense of the addition to the density of a pure solvent due to dissolved substances

$$\rho(x, z, t) = A(x, z, t) + \frac{R_b}{R_a} B(x, z, t) + \frac{R_c}{R_a} C(x, z, t). \quad (2.29)$$

Finally, the only parameters which can be manipulated by an experimenter are the initial values of the reactant concentrations  $\gamma_a$  and  $\gamma_b$ .

Thus, by obtaining a full set of equations (2.15)–(2.19) with the boundary conditions (2.20a,b), (2.21a,b) and the initial conditions in the form of either (2.22a,b), (2.23a,b) or (2.25a,b), (2.26a,b), we have formulated the problem. Note that the reaction-induced buoyancy number  $K_\rho$  does not automatically appear in the governing equations (2.15)–(2.19) after they have been converted to a dimensionless form. We will define this parameter below.

### 2.5. Concentration-dependent diffusion

The CDD effect is key to this work. To evaluate the diffusion formulas for the pair  $\text{HNO}_3/\text{NaOH}$ , we have brought together all the known experimental data (Bratsun *et al.* 2015). Note that the data on the concentration dependence of the diffusion coefficients have appeared to be fragmentary and incomplete for most substances. Therefore, we were forced to conduct our experiments to measure the diffusion coefficients (see data presented in Mizev *et al.* 2021). We assume for simplicity that the data set falls in the experimentally interesting range of concentration on a straight line  $f(X) = a + bX$ , where  $X$  stands for concentration,  $a$  and  $b$  are some constants. We suppose here that each diffusion coefficient depends only on the concentration of its substance. These linear laws in a dimensionless form, then, are

$$\left. \begin{aligned} D_a(A) &\approx 0.881 + 0.158A, \\ D_b(B) &\approx 0.594 - 0.087B, \\ D_c(C) &\approx 0.478 - 0.284C. \end{aligned} \right\} \quad (2.30)$$

Equations (2.30) perfectly approximate the diffusive properties within the concentration range from 0.1 up to  $A_{lim} = 3 \text{ mol l}^{-1}$ . The dimensionless table values for diffusion coefficients are as follows:

$$D_a^{tab} = 1.0, \quad D_b^{tab} = 0.68, \quad D_c^{tab} = 0.5, \quad (2.31a-c)$$

where the coefficients were scaled using  $D_{a0}$ .

One can see that the results of (2.30) for the limiting case of zero concentration do not coincide with the table values (2.31a-c). This is explained by the fact that the experimental

dependencies of the diffusion coefficients at small concentrations are strongly nonlinear. Since the neutralization reaction under ideal mixing runs fast, we can neglect these nonlinear effects at low concentrations.

### 3. Base-state solution

#### 3.1. Potential barrier and well

The problem (2.15)–(2.26a,b), (2.30) has an unsteady solution, which describes the reaction–diffusion processes. The fluid remains at mechanical equilibrium. We will consider this solution as a base-state solution. We assume that the fluid velocity equals zero in (2.15)–(2.19) and that the concentration fields depend only on the vertical coordinate and time:  $A^0(z, t)$ ,  $B^0(z, t)$ ,  $C^0(z, t)$ . The resulting time-dependent nonlinear equations

$$\frac{\partial A^0}{\partial t} = D_a(A^0) \frac{\partial^2 A^0}{\partial z^2} + \frac{dD_a(A^0)}{dA^0} \left( \frac{\partial A^0}{\partial z} \right)^2 - DaA^0B^0, \quad (3.1)$$

$$\frac{\partial B^0}{\partial t} = D_b(B^0) \frac{\partial^2 B^0}{\partial z^2} + \frac{dD_b(B^0)}{dB^0} \left( \frac{\partial B^0}{\partial z} \right)^2 - DaA^0B^0, \quad (3.2)$$

$$\frac{\partial C^0}{\partial t} = D_c(C^0) \frac{\partial^2 C^0}{\partial z^2} + \frac{dD_c(C^0)}{dC^0} \left( \frac{\partial C^0}{\partial z} \right)^2 + DaA^0B^0 \quad (3.3)$$

should be complemented with the boundary and initial conditions (2.20a,b)–(2.26a,b) and the formulas for CDD (2.30). This problem has no analytical solution and can only be solved numerically.

Figure 2 presents the base-state profiles of the density  $\rho^0(z, t)$  for four consecutive times  $t = 0, 2, 5, 10$ . We consider three fundamentally different cases. Figure 2(a) illustrates the situation when, the solutions being brought into contact, do not react ( $Da = 0$ ). In this case, one can observe a typical profile of the DLC instability, which occurs when the system is initially statically stable, and the fastest diffusing solute is in the upper layer. One can see here that a sharp drop in the density of the solutions given at the very beginning is gradually smoothed out since diffusion is a typical relaxation process.

Figure 2(b) shows the dynamics of the density profile starting from the same initial conditions, but now the solutions of  $\text{HNO}_3$  and  $\text{NaOH}$  react according to the equation (2.1). The CDD effect (2.30) is here not taken into account. Instead, the equations are integrated with constant tabular values (2.31a–c) for the diffusion coefficients. One can see that the situation does not change qualitatively, but the profiles become non-symmetric concerning the  $z$ -axis. However, the main feature of the density profile, to spread out over time under the influence of the relaxation process, has been preserved.

Finally, figure 2(c) shows the density evolution taking into account the CDD effect. A qualitative change here is the appearance of a potential barrier on the density profile. For this reason, the density profile has two minima above and below the reaction. It is interesting to note that the height and width of the potential barrier vary very little with time. This implies that the barrier is the result of an exact balance between CDD and the nonlinear chemical reaction.

Figure 3 shows the relative contributions of acid, base and salt to the total density  $\rho^0(z, t)$  of the medium. One can see that the reaction product makes a decisive contribution to the emergence of a potential barrier. Due to the barrier, which successfully resists the relaxation process, a potential well that is statically quasi-stable in time also arises in the system. Since gravity is anti-directed to the  $z$ -axis, only the potential well can exist

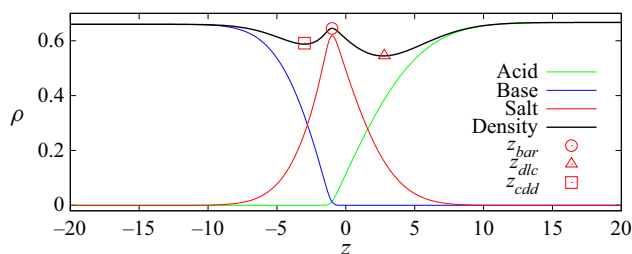


Figure 3. Base-state profiles of acid  $A^0$ , base  $B^0$  and their salt  $C^0$  showing contributions of species to the total density  $\rho^0$ . The initial concentrations are  $\gamma_a = 0.667$ ,  $\gamma_b = 0.55$ . All profiles are shown for time  $t = 5$ . The position of the potential barrier is indicated by the circle.

(the region to the left of the barrier in figure 3). The bottom of the potential well is marked with an open square. In this case, the potential barrier prevents the low-density area from floating up under the action of the Archimedes force. The low-density region to the right of the barrier is statically unstable and can float under the action of a buoyancy force. It is interesting to note that the well's depth almost does not change with time, yet its width increases time as the left wall is gradually smoothed out due to diffusion (see figure 2c).

Thus, the neutralization reaction, coupled with the CDD, can result in a potential well and maintain it for a long time in a quasi-steady state. As we will show below, this ability provides completely new opportunities for pattern formation scenarios in the system.

### 3.2. Stability map based on the base-state density profiles

We found that the stability map of the principal reaction–diffusion–convection modes observed experimentally (Mizev *et al.* 2021) can be constructed by analysing changes in the base-state density profile  $\rho^0(z, t)$  calculated using (3.1)–(3.3). Figure 4 presents this map in the parameter plane of the initial values for the concentrations of acid  $\gamma_a$  and base  $\gamma_b$  defined by (2.24a,b).

The relation (2.29) implies that the weight of an elementary volume of liquid depends both on the structure of the solute's molecule and on the amount of solute. Therefore, the condition

$$\gamma_b = \frac{\beta_a}{\beta_b} \gamma_a = \frac{R_a}{R_b} \gamma_a \quad (3.4)$$

on the stability map gives a line of equal density for the upper and lower layers, that is, an isopycnal line (thick solid line in figure 4). If the parameters are taken above the isopycnal line, then the base solution is heavier than the acid solution. Since we do not consider here the RT instability, this means that a less dense fluid lies above a denser fluid in a gravity field. Therefore, the intersection of the isopycnal line (3.4) means that the solutions change places.

After bringing the solutions of  $\text{HNO}_3$  and  $\text{NaOH}$  into contact, the reaction–diffusion processes transform the density profile and may cause potentially unstable conditions for the system under the gravity force. Density transformations under different initial concentrations are shown in figure 5. This figure presents typical density profiles that correspond to a vertical slice indicated in figure 4, which includes the main areas above and below the isopycnal line. Let us discuss the characteristic areas of the stability map in more detail. The upper left part of the map corresponds to the parameters at which the DLC instability arises (the solution with a faster diffusing substance is at the top). As a rule,

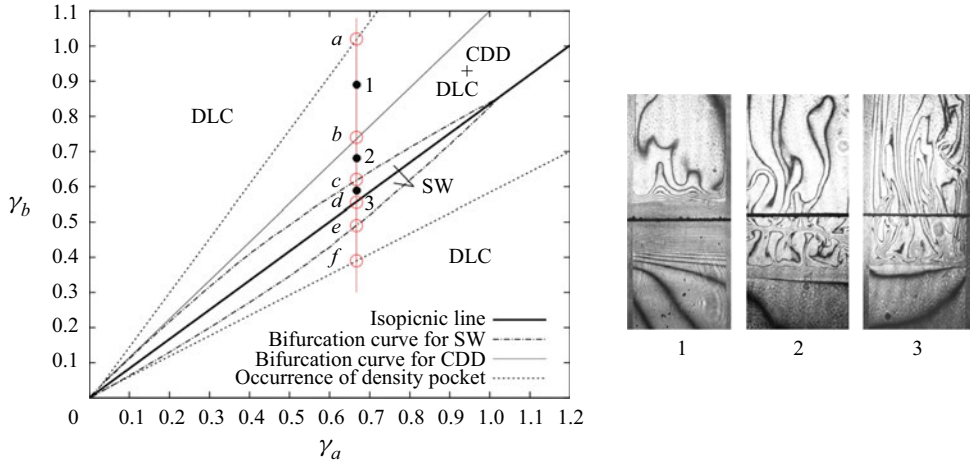


Figure 4. Stability map constructed by inspection of variations of the base-state density profile in the  $(\gamma_a, \gamma_b)$  parameter space. Abbreviations DLC, SW and CDD denote the diffusive layer convection (1), shock wave (3) and convection of CDD (2), respectively. The characteristic cross-section  $\gamma_a = 0.667$  of the stability map is indicated by a red straight line and discussed in figures 5 and 6 in more detail. Experimental interferograms (Mizev *et al.* 2021) are shown alongside to illustrate the main modes indicated in the map.

with no reaction, it is a formation of two areas with weak convective movements divided by a diffusion zone where the fluid remains motionless. The zones above and below are characterized by the system of fingers which propagate symmetrically up and down from the mixing zone (Trevelyan *et al.* 2011). It is known that the running reaction could violate the symmetry of the fingering process, giving preference to fingers that extend up or down (Almarcha *et al.* 2010). However, the effect of the reaction on the mass transfer processes in the system can be much more radical (Bratsun *et al.* 2015, 2017).

Moving down along the red line  $\gamma_a = 0.667$  shown in figure 4, we first cross the point *a*, which corresponds to the appearance of a new local maximum on the density curve (figure 5*a*). The reason is that the diffusion rate of salt decreases with the concentration increase (see (2.30)), which results in local accumulation of the reaction product near the initial contact surface of the solutions. Also, since the salt is quite heavy, its contribution to the density (2.29) is significant. Thus, the density maximum indicates where the reaction product accumulates in the system and serves as an indicator for the reaction front location. The appearance of a potential well, or in other words ‘a density pocket’, in figure 5(*a*) does not mean the immediate development of convection there. For this, the local Rayleigh number must exceed its critical value. Let us define this parameter as follows:

$$R_{local} = \frac{1}{R_{local}^{cr}} \frac{g\beta_c N d^4}{16\nu D_{c0}}, \quad (3.5)$$

where  $D_{c0}$  is the table value of the diffusion coefficient of salt,  $N$  is the characteristic linear gradient of salt concentration in a potential well and  $d$  is the width of the potential density well. The semi-width  $d/2$  is chosen as the characteristic size because the instability condition is fulfilled only in one half of the potential well. It can be calculated as

$$\frac{d}{2} = |z_{bar} - z_{cdd}| \quad (3.6)$$

(see figure 3 for details). The parameter  $R_{local}$  is normalized by its critical value  $R_{local}^{cr}$ , which could be either calculated within a linear stability analysis or taken from a

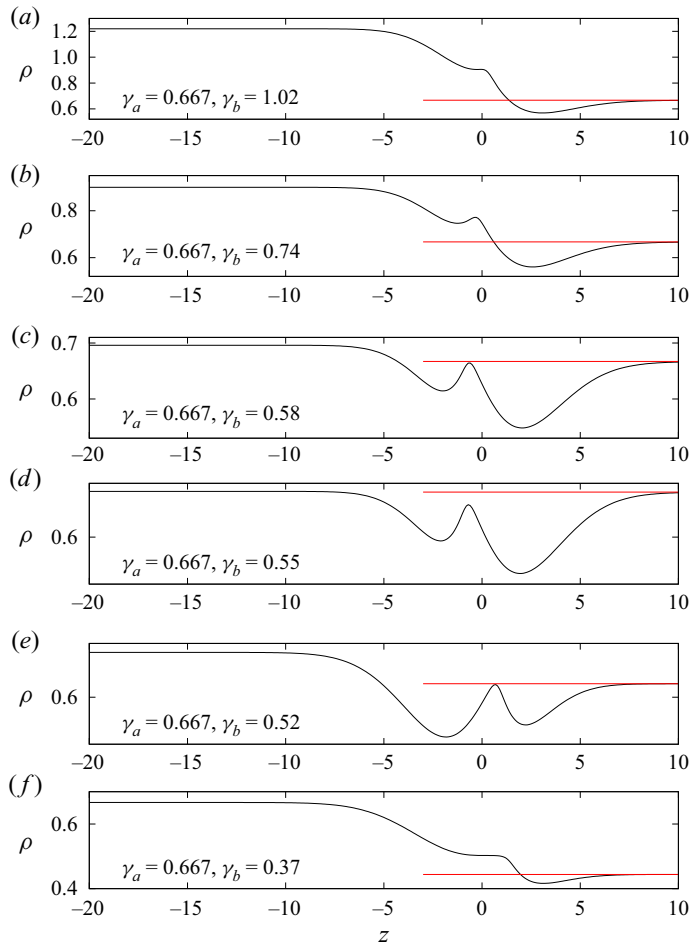


Figure 5. Instantaneous density profiles  $\rho^0(z, t)$  for the reaction–diffusion base state calculated for different values of the control parameters  $\gamma_a$  and  $\gamma_b$  marked on the stability map (see figure 4). Red horizontal lines are drawn for the convenience of comparing the reaction zone and upper layer densities. The position of the initial contact surface of the solutions is determined by  $z = 0$ . All profiles are shown for time  $t = 5$ .

textbook on the solutal Rayleigh–Bénard problem (Gershuni & Zhukhovitskii 1976). In the definition (3.5), we also take into account the fact that the main contribution to the appearance of the potential well is made by the reaction product.

The variation of  $R_{local}$  as a function of  $\gamma_b$  and fixed  $\gamma_a = 0.667$  is shown in figure 6(a). It is seen that the fluid loses its stability with respect to local perturbations limited to the density pocket at approximately  $\gamma_b = 0.73$  (point *b* in figure 4). The corresponding density profile is presented in figure 5(b). We have called this type of instability CDD convection, emphasizing the fact that, without the effect of CDD, convection in the potential well would not have been possible. To demonstrate this, figure 6(a) also presents the curve calculated without taking into account the CDD effect. Although the local Rayleigh number slightly exceeds the critical value of 1 near the isopycnal line itself, this instability still does not occur because, in this parameter range, the system becomes unstable to another type of perturbation (see below). In fact, the potential well, where the



Buoyancy-driven flows induced by a neutralization reaction

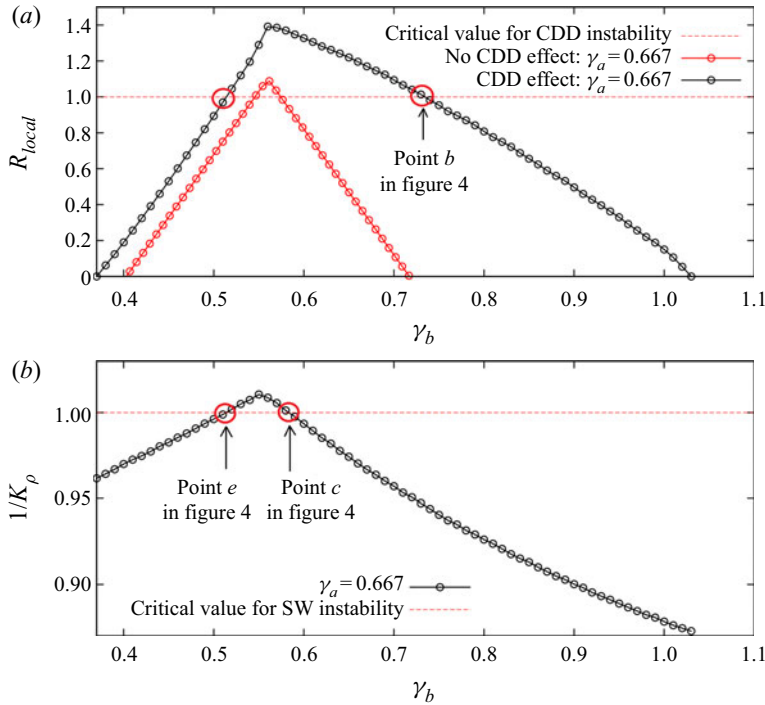


Figure 6. Variation of the local Rayleigh number calculated inside a potential well (a) and the inverse of the reaction-induced buoyancy number  $K_\rho$  (b) as a function of the dimensionless initial concentration of base  $\gamma_b$ . The corresponding cross-section of the stability map is given in figure 4. The critical value of the parameter in each case is indicated by a red dashed line (instability above the line).

CDD instability occurs, is destroyed by a global bifurcation and begins to float upward together with the entire reaction zone.

By inspecting the critical density profile shown in figure 5(b), we can conclude the reaction zone density is still less than the density of the lower layer, but higher than that of the upper layer. This allows the DLC and CDD instabilities to coexist together while being separated by a thin diffusive layer.

Moving further down along the red line in figure 4, we cross the point c ( $\gamma_b \approx 0.58$ ), where the densities of the reaction zone and the upper layer become equal. In what follows, for convenience, we define the reaction-induced buoyancy number  $K_\rho$  introduced in Mizev *et al.* (2021) as

$$K_\rho = \begin{cases} \frac{1 + A^0(z_{bar}, t_c) + \frac{R_b}{R_a} B^0(z_{bar}, t_c) + \frac{R_c}{R_a} C^0(z_{bar}, t_c)}{1 + A^0(H, t_c)}, & \text{if acid is above base;} \\ \frac{1 + A^0(z_{bar}, t_c) + \frac{R_b}{R_a} B^0(z_{bar}, t_c) + \frac{R_c}{R_a} C^0(z_{bar}, t_c)}{1 + \frac{R_b}{R_a} B^0(H, t_c)}, & \text{if base is above acid,} \end{cases} \quad (3.7)$$

where  $z_{bar}$  stands for the position of the local maximum density in the reaction zone (it coincides with the position of the potential barrier, see figure 3),  $t_c$  is the point in time

when the density measurement occurs. Generally, the measurement should be carried out in the limit of the large time asymptotic solution  $t_c \rightarrow \infty$ . In practice, the parameter (3.7) was calculated for a sufficiently long time  $t_c = 10$ .

In figure 6(b), we show the variation of  $1/K_\rho$  as a function of  $\gamma_b$  and fixed  $\gamma_a = 0.667$ . The density profile in figure 5(c) indicates that this is the point for global bifurcation in the system, at which an intense convective motion in the form of a shock wave occurs (Bratsun *et al.* 2017). It can be noted that the area limited by the curve  $K_\rho = 1$  is a narrow band pressed to the isopycnal line. The area becomes narrower and fades away at both small and comparatively large values of the initial concentrations. The estimates show that at  $\gamma_a > 1$  the effect disappears.

Moving further along the parameter plane, we pass over the isopycnal line at  $\gamma_b = 0.55$  (the point *d* in figure 4) and enter the parameter area where the acid and base solutions change places. Figure 6(b) demonstrates that, below the isopycnal line, there is also a region of intense convective motion. The exit from this mode occurs at the point *e* ( $\gamma_b \approx 0.52$ ). The corresponding density profile is shown in figure 5(e).

It is important to show why the CDD convection does not occur if the acid and base change places in the system (below the isopycnal line in figure 4). Figure 5 clearly demonstrates that the bifurcation points for the onset of the CDD and SW instabilities practically coincide. Due to this, the CDD convection, which is principally local, does not have a chance to develop. Ultimately, this happens because of the asymmetry of the local maximum with respect to the up–down reflection, which is the result of different diffusion rates of  $\text{HNO}_3$  and  $\text{NaOH}$ . The slope of the potential wall located on the side of the base solution is always greater since the diffusion rate of nitric acid in the water is higher (for example, compare the profiles shown in the figure 5c,e). Thus, chemoconvective cells cannot arise, although the potential well supported by the CDD effect and nonlinear reaction continues to exist between the points *e* and *f* in figure 4.

#### 4. Linear stability analysis

Although in the previous section we have been able to build a stability map based only on the analysis of the base-state density profiles, it makes sense to analyse the stability of a time-dependent base state with respect to small perturbations. The appearance of a potential well on the density profile (figure 5) provides the necessary, but not sufficient, conditions for the onset of instability.

There are two methods commonly used to determine the stability of a time-dependent flow. The first one is the quasi-steady-state approximation (QSSA) method, in which one freezes the time and determines the growth constant as if the base state were steady. The second method is the initial value problem (IVP) for small disturbances. The former method neglects the rate of change of the base state and leads to an eigenvalue problem with time appearing as a parameter. The second method is an exact solution for the IVP, which brings the initial data into consideration. Tan & Homsy (1986) have shown for viscous fingering problems that the IVP calculation gives essentially the same results as the QSSA approach, except for a short time when the base state changes rapidly. The difference between the methods is that, at the very beginning of evolution, the growth rate of disturbances within the IVP calculations is always negative because the development of the instability takes time.

Generally, there is a considerable list of papers devoted to linear stability analysis in different time-dependent problems with a non-monotonic density profile (see Manickam & Homsy 1993, 1995; Loggia *et al.* 1995; Loggia, Salin & Yortsos 1998; Loggia *et al.*

1999; Martin *et al.* 2002; Hejazi *et al.* 2010; Trevelyan *et al.* 2011; Hejazi & Azaiez 2012; Gandhi & Trevelyan 2014; Kim 2014; Trevelyan *et al.* 2015; Bratsun 2019; Kim 2019).

Earlier work provides examples of analysis in viscous fingering systems. For example, Loggia *et al.* (1995, 1998) studied the stability of the downdip displacement in a porous medium of a dense and viscous fluid by a lighter and less viscous fluid, and *vice versa* using an acoustic technique. They found that conventional predictions based on a long-wave (LW) theory lead to identical instability thresholds for the two flows, while a short-wave (SW) analysis suggests that instability sets in earlier than the LW predictions and leads the two different thresholds. Manickam & Homsy (1993) and Manickam & Homsy (1995) employed a linear theory using the QSSA to study the effect of a non-monotonic viscosity profile on the stability of miscible displacements in a porous medium. The important finding was that the diffusion of the base state does not always mitigate the instabilities and the small wavenumber expansion gives a sufficient condition for the flow to be unstable. Generally, the assumption of an especially designed density profile (step like) allows one to obtain an analytical solution (or quasi-analytical solution) for time  $t = 0$  by applying the QSSA method. In special cases, it is possible to obtain an exact solution for later times, for example, in the absence of dispersion and diffusion (Hickernell & Yortsos 1986). However, in the general case, at late times  $t > 0$ , the density profile changes irreversibly, the constructed initial state is destroyed and the problem can only be solved numerically. In the case of a reaction with nonlinear kinetics and/or nonlinear diffusion, researchers are faced with the problem of obtaining a closed-form solution for the base state since the system should be solved numerically already in the main order of expansion. There are few examples of exact solutions (Hejazi *et al.* 2010; Kim 2014), but they are valid for very special cases of reactions and initial concentrations of reactants.

#### 4.1. Analytical QSSA solution for the simplified problem

In our problem, an initially stable density profile evolves to a state with a potential well. One can see in figure 2(c) that the density profile changes rapidly at the very beginning and then slowly evolves, but does not change qualitatively. We can use this property employing a linear theory analytically within the QSSA approach.

Let us consider the following simplified system of equations:

$$\Phi + \nabla^2 \Psi = 0, \quad (4.1)$$

$$\nabla^2 \Phi - 12\Phi - \frac{\partial \rho}{\partial x} = 0, \quad (4.2)$$

$$\frac{\partial \rho}{\partial t} + \frac{\partial \Psi}{\partial z} \frac{\partial \rho}{\partial x} - \frac{\partial \Psi}{\partial x} \frac{\partial \rho}{\partial z} = \nabla^2 \rho, \quad (4.3)$$

where  $\rho$  is the density of the medium. The variables in (4.1)–(4.3) were rescaled in such a way that the diffusion coefficient and Rayleigh number were removed from the equations (Hejazi *et al.* 2010; Gandhi & Trevelyan 2014). We neglect the processes of reaction and nonlinear diffusion in (4.3). To simplify the analysis, we replace the reaction–diffusion equations generating a non-monotonic density profile by the initial state in the form of a rectangular potential well, which slowly (in terms of the development of hydrodynamic

disturbances) expands with time

$$\rho^0(\tau, z) = \begin{cases} 0, & z > d(\tau) \\ -D, & 0 \leq z \leq d(\tau) \\ 0, & z < 0 \end{cases}, \quad (4.4)$$

where  $d$  stands for the width of the potential well changing over slow time  $\tau$ ,  $D$  is the constant well depth. The density profile constructed from a linear combination of step functions as in (4.4) allows us to obtain the closed-form analytical solution (Tan & Homsy 1986; Gandhi & Trevelyan 2014).

We decompose the small monotonic perturbations in the following way:

$$\begin{pmatrix} \Phi(t, x, z) \\ \Psi(t, x, z) \\ \rho(t, x, z) \end{pmatrix} = \begin{pmatrix} 0 \\ 0 \\ \rho^0(\tau, z) \end{pmatrix} + \begin{pmatrix} \varphi(z) \\ \psi(z) \\ a(z) \end{pmatrix} \exp(\sigma t + Ikx), \quad (4.5)$$

where  $\varphi, \psi, a$  are, respectively, the amplitudes of normal mode perturbations for the vorticity, streamfunction and density;  $k$  is the wavenumber and  $\sigma$  is the growth rate.

Substituting (4.5) into (4.1)–(4.3) and linearizing these equations near the base state (4.4), we obtain the following system of amplitude equations for the determination of critical perturbations:

$$\varphi + \frac{d^2\psi}{dz^2} - k^2\psi = 0, \quad (4.6)$$

$$\frac{d^2\varphi}{dz^2} - (k^2 + 12)\varphi - k^2a = 0, \quad (4.7)$$

$$\sigma a = \frac{d^2a}{dz^2} - k^2a - \psi \frac{d\rho^0}{dz}. \quad (4.8)$$

Equations (4.6)–(4.8) should be supplemented by the condition that the solutions are continuous at the jumps

$$\left. \begin{aligned} z = 0, d(\tau) : \quad & [\psi]_-^+ = 0, \quad [\varphi]_-^+ = 0, \quad [a]_-^+ = 0, \\ & \left[ \frac{d\psi}{dz} \right]_-^+ = 0, \quad \left[ \frac{d\varphi}{dz} \right]_-^+ = 0, \quad \left[ \frac{da}{dz} + \psi \rho^0 \right]_-^+ = 0. \end{aligned} \right\} \quad (4.9)$$

The sixth-order system of ordinary differential equations (4.6)–(4.8) can be analytically solved for three spatial ranges (inside and outside the potential well). The obtained solutions then are substituted into the jump conditions (4.9), yielding a linear system of twelve algebraic equations for the unknowns. We should require that the determinant  $12 \times 12$  coefficient matrix be equal to zero, which results in the dispersion equation

$$\begin{aligned} \frac{24\sigma^2(\sigma - 12)^2}{D^2k^2} &= \frac{k}{l}(\sigma - 12) \left(1 - e^{-(k+l)d}\right) - \frac{k\sigma}{12m}(\sigma - 12) \left(1 - e^{-(k+m)d}\right) \\ &\quad - \frac{k^2\sigma}{ml} \left(1 - e^{-(l+m)d}\right) + \frac{6k^2}{l^2} \left(1 - e^{-2ld}\right) + \frac{k^2\sigma^2}{24m^2} \left(1 - e^{-2md}\right) \\ &\quad + \frac{(\sigma - 12)^2}{24} \left(1 - e^{-2kd}\right), \end{aligned} \quad (4.10)$$

where  $l^2 \equiv k^2 + \sigma$ ,  $m^2 \equiv k^2 + 12$ .

*Buoyancy-driven flows induced by a neutralization reaction*

The equation for the cutoff wavenumber  $k$  is then obtained in the limit  $\sigma \rightarrow 0$

$$d^2 D^2 = \frac{2304k^2 d^2}{F_1 + F_2 (1 - e^{-(k+m)d}) - F_3 e^{-2kd} + F_4 (1 - e^{-2md})}, \quad (4.11)$$

where

$$\left. \begin{aligned} F_1 &= 1 - \frac{1}{3}k^2 - \frac{12d - m}{36m}k^4, & F_2 &= \frac{k^3}{3m} \left( 1 + dk - \frac{1}{6}k^2 \right) \\ F_3 &= 1 + 2dk + \frac{2d^2 - 1}{3}k^2 - \frac{H}{3}k^3 + \frac{1}{36}k^4, & F_4 &= \frac{k^6}{36(k^2 + 12)}. \end{aligned} \right\} \quad (4.12)$$

Let us determine the condition for the instability onset in the LW limit expanding the cutoff condition (4.11) for small  $k$

$$\left( -6d^2 + \frac{13824}{D^2} \right) k^2 + \left( 2d - \frac{2}{m} + \frac{2}{me^{md}} + 4d^3 \right) k^3 + \dots \quad (4.13)$$

To leading order in  $k$ , we obtain the important relation for the threshold

$$d(\tau) > \frac{48}{D}. \quad (4.14)$$

We can compare our result with the analytical result obtained by Tan & Homsy (1986) and Gandhi & Trevelyan (2014) for initial time  $t = 0$  in the case of the Darcy motion equation

$$d > \frac{4}{D}. \quad (4.15)$$

Our analysis (4.14) is applicable at any time. At the very beginning of evolution, the width of the potential well is extremely small; therefore, LW disturbances will not be excited. We should expect that the most dangerous disturbances will be short waves (SW). Comparing (4.14) and (4.15), we can conclude that taking into account the Brinkman term results in the fact that LW disturbances are successfully damped.

#### 4.2. Numerical IVP solution

In our case, the instability always develops after some critical time and the IVP usage is more reasonable. Let us decompose the small monotonic perturbations in the following way:

$$\begin{pmatrix} \Phi(t, x, z) \\ \Psi(t, x, z) \\ A(t, x, z) \\ B(t, x, z) \\ C(t, x, z) \end{pmatrix} = \begin{pmatrix} 0 \\ 0 \\ A^0(t, z) \\ B^0(t, z) \\ C^0(t, z) \end{pmatrix} + \begin{pmatrix} \hat{\phi}(t, z) \\ \hat{\psi}(t, z) \\ a(t, z) \\ b(t, z) \\ c(t, z) \end{pmatrix} e^{ikx}, \quad (4.16)$$

where  $\hat{\phi}$ ,  $\hat{\psi}$ ,  $a$ ,  $b$ ,  $c$  are, respectively, the amplitudes of normal mode perturbations for the vorticity, streamfunction, acid, base and salt concentrations while  $k$  is their wavenumber.

Substituting (4.16) into (2.15)–(2.19) and linearizing these equations near the base state (3.1)–(3.3), we obtain the following system of time-dependent amplitude equations for the determination of critical perturbations:

$$\varphi + \frac{\partial^2 \psi}{\partial z^2} - k^2 \psi = 0, \tag{4.17}$$

$$\frac{1}{Sc} \frac{\partial \varphi}{\partial t} = \frac{\partial^2 \varphi}{\partial z^2} - (k^2 + 12)\varphi - k^2(Ra_a a + Ra_b b + Ra_c c), \tag{4.18}$$

$$\begin{aligned} \frac{\partial a}{\partial t} = & D_a(A^0) \left( \frac{\partial^2 a}{\partial z^2} - k^2 a \right) + \frac{dD_a(A^0)}{dA^0} \left( 2 \frac{\partial A^0}{\partial z} \frac{\partial a}{\partial z} + a \frac{\partial^2 A^0}{\partial z^2} \right) \\ & - Da(A_0 b + a B_0) - \psi \frac{\partial A^0}{\partial z}, \end{aligned} \tag{4.19}$$

$$\begin{aligned} \frac{\partial b}{\partial t} = & D_b(B^0) \left( \frac{\partial^2 b}{\partial z^2} - k^2 b \right) + \frac{dD_b(B^0)}{dB^0} \left( 2 \frac{\partial B^0}{\partial z} \frac{\partial b}{\partial z} + b \frac{\partial^2 B^0}{\partial z^2} \right) \\ & - Da(A_0 b + a B_0) - \psi \frac{\partial B^0}{\partial z}, \end{aligned} \tag{4.20}$$

$$\begin{aligned} \frac{\partial c}{\partial t} = & D_c(C^0) \left( \frac{\partial^2 c}{\partial z^2} - k^2 c \right) + \frac{dD_c(C^0)}{dC^0} \left( 2 \frac{\partial C^0}{\partial z} \frac{\partial c}{\partial z} + c \frac{\partial^2 C^0}{\partial z^2} \right) \\ & + Da(A_0 b + a B_0) - \psi \frac{\partial C^0}{\partial z}, \end{aligned} \tag{4.21}$$

where  $\psi \equiv -Ik\hat{\psi}$ ,  $\varphi \equiv -Ik\hat{\varphi}$ . Equations (4.17)–(4.21) should be supplemented by the boundary conditions for disturbances

$$z = \pm H : \quad \psi = 0, \quad \varphi = 0, \quad \psi = 0 \quad \frac{\partial a}{\partial z} = 0, \quad \frac{\partial b}{\partial z} = 0, \quad \frac{\partial c}{\partial z} = 0. \tag{4.22a-e}$$

To find stability conditions, the equations for disturbances (4.17)–(4.21) and (4.22a–e) are numerically integrated together with the equations for the base state (3.1)–(3.3) to compute the growth rate  $\lambda_L(z, t)$  for a given wavenumber  $k$ . Repeating the calculations for varying  $k$  enables us to describe the growth of small disturbances over a range of wavenumbers. As is known, the growth rate for time-dependent stability problems can be defined in a different way. Based on the fact that the acid in the system is the most active agent, we define the growth rate similar to a Lyapunov exponent

$$\lambda_L(z_0, t) = \frac{1}{N} \sum_{j=1}^N \frac{1}{\Delta t} \ln \frac{a_j(t + \Delta t, z_0)}{a_j(t, z_0)}, \tag{4.23}$$

where  $\Delta t$  is the integration time step and  $N$  is the number of independent realizations (typically 10–15). Because  $\lambda_L$  is sensitive to the given initial data, each independent integration starts from white noise with an amplitude of less than  $10^{-4}$ . We fix the occurrence of instability to the time when  $\lambda_L(t)$  averaged over  $N$  realizations changes sign from negative to positive. The integration time step  $\Delta t$  is not constant and changes in accordance with the Courant rule so that the explicit scheme would be stable.

We can apply a linear analysis only to instabilities that develop locally. For example, the SW convection occurs after a global bifurcation, which looks like a catastrophe for



Buoyancy-driven flows induced by a neutralization reaction

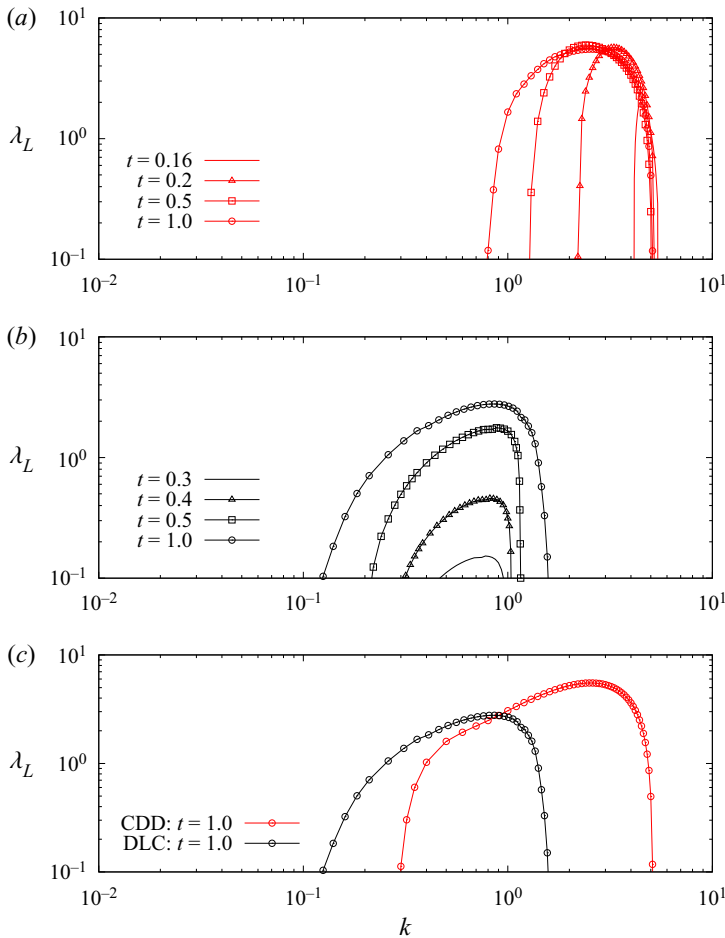


Figure 7. Real parts of the growth rate  $\lambda_L$  of the pure CDD instability (a), the pure DLC instability (b) and the mixed-mode instability (c) are illustrated at different times. The initial concentrations are  $\gamma_a = 0.667$ ,  $\gamma_b = 0.66$ .

the system. Obviously, the study of stability boundaries for infinitesimal perturbations, in this case, does not make sense. Therefore, we can only investigate the development of the CDD and DLC instabilities. Thus, it is convenient to calculate the growth rate of the CDD and DLC disturbances respectively as  $\lambda_L(z_{cdd}, t)$  and  $\lambda_L(z_{dlc}, t)$ , i.e. at points  $z_{cdd}$  and  $z_{dlc}$ , which coincide with two minima of the density profile (see figure 3).

Figure 7(a) presents the instantaneous growth rates  $\lambda_L(z_{cdd}, t)$  as a function of the wavenumber  $k$  calculated for the CDD convection. This instability develops below the initial contact surface. The minimum of the neutral curve corresponds to the wavenumber  $k_{cdd} \approx 4.4$  at time  $t_1 \approx 0.156$ . The figure shows the development of a pure type of instability, which is not affected by other disturbances. This is achieved by considering only those perturbations that are localized inside the potential well. All other disturbances during the calculation have been artificially nullified. Figure 7(b) presents the growth rates  $\lambda_L(z_{dlc}, t)$  calculated for the pure DLC instability developing above the initial contact surface. This instability starts at  $k_{dlc} \approx 0.75$  and  $t_2 \approx 0.253$ .

Although the potential barrier in the form of dense immobile fluid separates the sublayers where two instabilities develop, the instabilities still can influence each other through a diffusion mechanism. To demonstrate the mode interaction, we have recalculated the growth rate curve for both modes, allowing any disturbances to develop in the system. Figure 7(c) presents the growth rates  $\lambda_L(z_{cdd}, t)$  and  $\lambda_L(z_{dlc}, t)$  for  $t = 1$ . In this case, the instability region for the CDD convection has significantly expanded due to the longer modes. The DLC mode develops exactly in the same wavelength range. Thus, the influence of the DLC on the CDD instability looks obvious. It is provided by a relatively mobile acid, which easily penetrates the potential barrier and invades the potential well. Thus, it is the acid diffusion that is responsible for the nonlinear mixed-mode instability. To be precise, the DLC instability develops almost independently, since the low-mobility salt and base cannot penetrate the potential barrier separating the sublayers.

## 5. Numerical simulation

### 5.1. Numerical solution technique

The problem (2.24a,b)–(3.7) is solved numerically by a finite difference method. We consider the Hele-Shaw cell with aspect ratio almost as in the experimental cuvette:  $L = 20$ ,  $H = 37$  (20 per 74 units of dimensionless length). The equations and boundary conditions are approximated on a rectangular uniform grid with  $101 \times 371$  nodes using a second-order approximation for the spatial coordinates. The one-sided and central differences are used to approximate the time and coordinate derivatives, respectively. The choice of this resolution is based on our previous experience with the numerical simulation of buoyancy-driven flows and is defined by the characteristic size of the arising structures (Bratsun *et al.* 2015, 2017). The nonlinear equations are solved using an explicit scheme. The Poisson equation is solved by the iterative Liebman successive over-relaxation method at each time step: the accuracy of the solution is fixed to  $10^{-4}$ . The initial condition for the velocity is determined by a random distribution of the streamfunction field with an amplitude of no more than  $10^{-3}$ .

Generally, a large Schmidt number allows us to omit the left part of the equation in (2.30). However, in terms of a numerical procedure, it is easier and more efficient to solve a non-stationary motion equation than to iterate while solving the Poisson equation. That is why a nonlinear term in (2.30) is not omitted, although this imposes a special condition on the time step

$$\Delta t = \frac{\Delta x^2}{2(2 + \max(|\Psi|, |\Phi|))}. \quad (5.1)$$

The following fixed parameters have been used for all the simulations performed in this paper:  $Sc = 317$ ,  $Da = 10^3$ ,  $R_a = 3.18 \times 10^5$ ,  $R_b = 3.82 \times 10^5$ ,  $R_c = 5.1 \times 10^5$ .

To characterize the nonlinear dynamics resulting from the coupling between chemical reactions and hydrodynamic flows, various types of measurements have been made during the numerical simulations. At successive times, the concentration fields can be spatially averaged along the transverse coordinate  $x$  to yield the averaged density profile

$$\rho_z(z, t) = \frac{1}{L} \int_0^L \left( A(x, z, t) + \frac{R_b}{R_a} B(x, z, t) + \frac{R_c}{R_a} C(x, z, t) \right) dx. \quad (5.2)$$

The transverse-averaged profile (5.2) gives information on the speed and intensity of the invasion of the reaction front and convective currents into the lower layer.

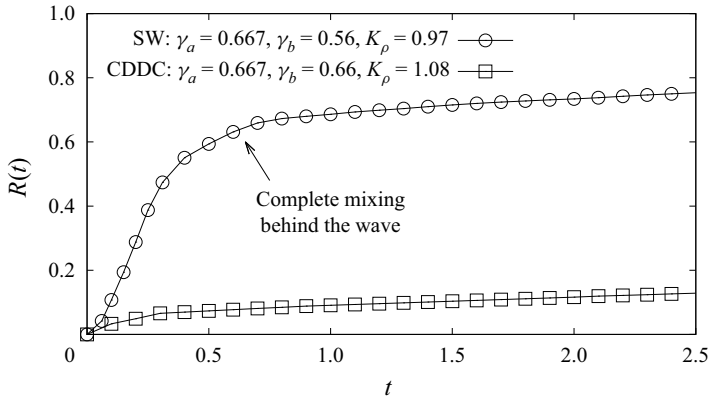


Figure 8. Variation of the integral reaction rate  $R$  as a function of time.

If the chemical reactions affect the fluid flows, then convection can also significantly affect the reaction rate, thus ensuring more intensive mixing of the reacting substances. In that respect, an important measurement is provided by the reaction rate computed in terms of the area of the reacted zone (i.e. the number of points where  $C(x, z, t)$  is larger than an arbitrary threshold  $C_0$ ) normalized by the area of the system  $2HL$  versus time

$$R(t) = \frac{1}{2HL} \int_{-H}^H \int_0^L \theta(C - C_0) dz dx, \quad (5.3)$$

where  $\theta$  stands for the Heaviside step function. This function returns zero everywhere, except for the areas with a salt concentration  $C$  exceeding  $C_0$ . In the latter case,  $\theta = 1$ . Typically, the threshold was defined to be  $C_0 = 10^{-3}$ .

In what follows, we present the results of direct numerical simulation of buoyancy-driven flows governed by (2.24a,b)–(3.7). We consider here two fundamentally different situations in which reaction–diffusion–convection processes occur under the control of convection ( $K_\rho < 1$ ) or under the control of diffusion ( $K_\rho > 1$ ).

### 5.2. Shock-wave convection

To be specific, we consider the case  $\gamma_a = 0.667$ ,  $\gamma_b = 0.56$  (between points  $c$  and  $d$  on the stability map shown in figure 4). Mass transfer processes in this area proceed under the control of convection, because the reaction zone is much lighter than the upper layer, and the estimate for the parameter (3.7) gives a value  $K_\rho = 0.97$ . Figure 8 shows changes in the integral reaction rate  $R(t)$  for this case. One can see that almost complete mixing of salt occurs already after the passage of half a unit of time after the solutions were brought into contact (approximately 150 s). This indicates the extremely intense mass transfer that occurs in the system and the large-scale movement of the fluid throughout the cell.

Figure 9 illustrates the evolution of the density profile obtained within a base reaction–diffusion state ( $t = 0.3$ ) and in the context of the nonlinear theory ( $t = 0.7, 2, 3$ ). If the linear theory makes it possible to demonstrate the structure of the reaction zone with two minima (see also figure 3), then the nonlinear evolution clearly shows the formation of a SW structure already at the early stage of the reaction–diffusion–convection processes. The pattern is formed as a result of the collapse of two depleted zones of low density. Finally, we note that the SW consists of two density levels with a thin transition region and moves towards a denser lower layer. This figure clearly demonstrates that the analysis of the

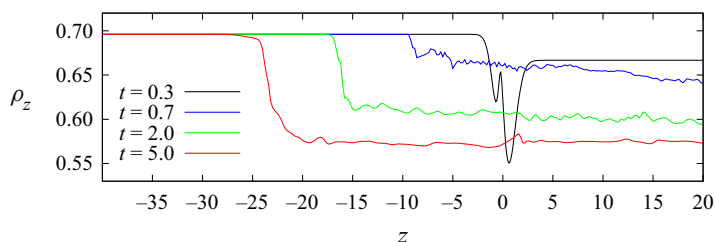


Figure 9. Time evolution of a transverse-averaged total density  $\rho_z(z, t)$  during the development of the SW convection. The initial concentrations are  $\gamma_a = 0.667$ ,  $\gamma_b = 0.56$ . The reaction-induced buoyancy number is  $K_\rho = 0.97$ .

base-state density profile, as well as the linear stability analysis associated with it, become meaningless. The SW mode is triggered as a result of a global bifurcation. It is interesting to note that the density profile at the bifurcation value  $K_\rho = 1$  can be represented as a homoclinic trajectory (see figure 5c).

Figure 8 clearly illustrates the fact that the system evolution passes through two qualitatively different stages. The first stage is characterized by the exponential growth of the mixing region. In the second stage, the mixing region grows monotonically. Figure 10 shows the density  $\rho$  for sequential time moments. The first SW formation stage is presented in (a). At the very beginning of the system evolution, when the convection is still not strongly involved in the mass transfer processes, the densities of the upper and lower layers away from the reaction zone are close to each other and the isopycnal line ( $\gamma_a = 0.667$ ,  $\gamma_b = 0.56$ ). Along with that, the reaction–diffusion processes create two layers of reduced densities which are formed from the burning out of the acid and base in the reaction zone, resulting in the accumulation of the heavy salt in the centre of the reaction zone. Since, with the value of the reaction-induced buoyancy number  $K_\rho < 1$ , the density of the reaction zone is lower than the density of the upper layer, the entire reaction zone almost immediately after bringing the fluids into contact begins to float up (see figure 10,  $t = 0.1$ ). One can see the formation of powerful plumes that emerge under the influence of the buoyancy force (figure 10,  $t = 0.3$ ).

The intense mode described above cannot last for a long time in a closed reactor. The continuous SW development requires a constant input of fresh reactants. Therefore, the evolution of the system becomes calm, which is illustrated in figure 10(b). After approximately  $t = 0.5$ , the upper part of the system becomes quasi-homogeneous, while the lower part, which does not participate in the convective movement, remains homogeneous (figure 10,  $t = 1$ ). The system is split into two zones with typical density values divided by the narrow transition zone. A reduced-weight reaction zone continues to be produced, floating up either at the edges of the cell or in certain places. Thus, the fresh acid continues to flow to the contact surface with the lower base layer. Finally, one can observe a SW structure with an almost planar front and nearly discontinuous change in density across the wavefront. This wave propagates fast compared to the characteristic diffusion times and separates the motionless fluid and the area with anomalously intense convective mixing (figure 10,  $t = 1.5, 2.5, 3, 3.5$ ).

### 5.3. CDD convection

If the control parameters are set so that the density of the reaction zone is higher than the density of the upper layer, then a completely different scenario for the development of

*Buoyancy-driven flows induced by a neutralization reaction*

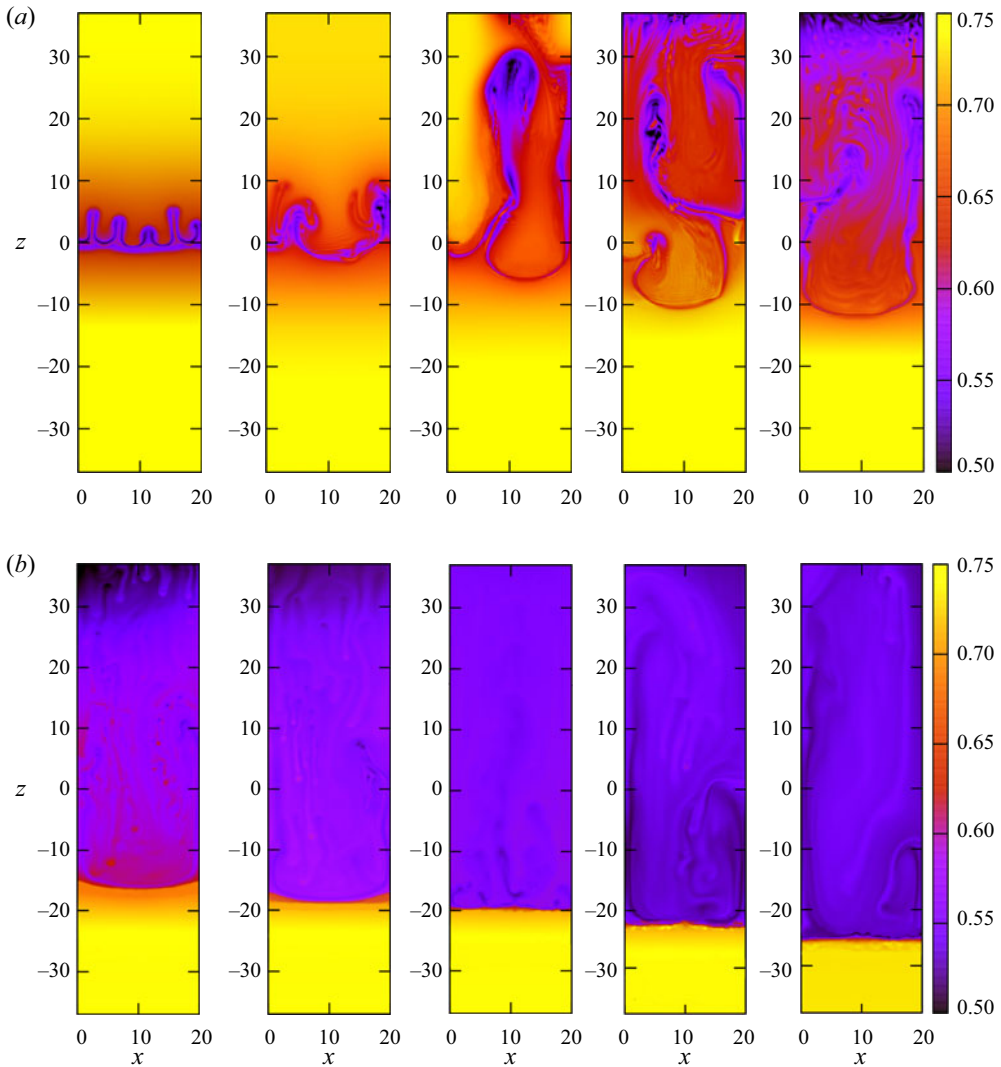


Figure 10. Evolution of the density  $\rho$  with time showing the development of the SW structure. The frames from left to right and from top to bottom correspond to times  $t = 0.1, 0.2, 0.3, 0.4, 0.5, 1.0, 1.5, 2.5, 3.0$  and  $3.5$ , respectively. The integration domain is  $0 \leq x \leq 20, -37 \leq z \leq 37$ . The initial concentrations are  $\gamma_a = 0.667, \gamma_b = 0.56$ . The reaction-induced buoyancy number is  $K_\rho = 0.97$ .

instability is observed. Figure 11 shows the dynamics of the density field for  $K_\rho = 1.08$  (between points *b* and *c* on the stability map shown in figure 4). Note that the system evolution begins with the base reaction–diffusion state, in which the fluid remains at mechanical equilibrium (figure 11,  $t = 1$ ). In this state, there is a local maximum located just below the initial contact line  $z = 0$ . Over time, two types of convective perturbation begin to grow in the system.

In the upper layer, favourable conditions are created for the initiation of the DLC instability, which usually occurs when two solutions are mixed with a rapidly diffusing solute at the top and slowly diffusing solute at the bottom. In this case, these are acid and salt, respectively.

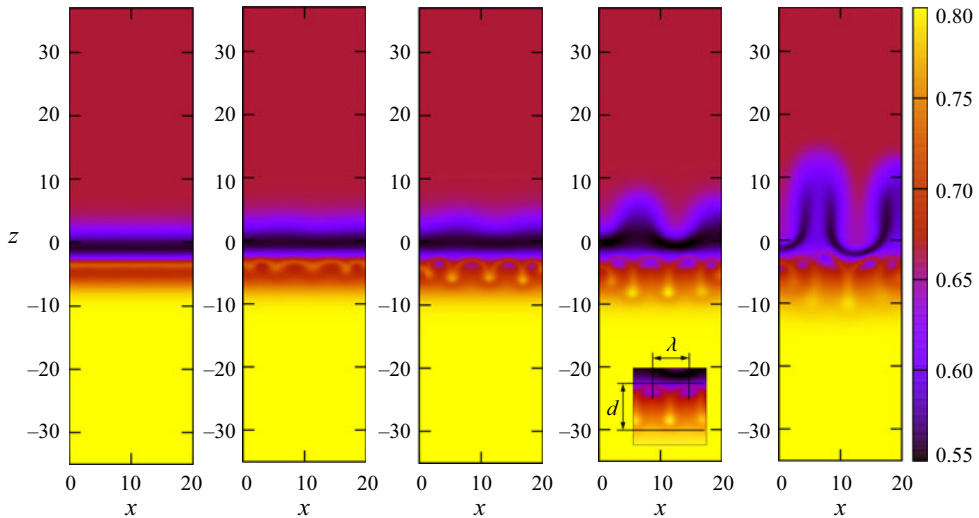


Figure 11. Evolution of the density  $\rho$  with time, showing the development of the CDD convection coupled with the DLC instability. The frames from left to right correspond to times  $t = 1, 2, 3, 4$  and  $5$ , respectively. The integration domain is defined by  $0 \leq x \leq 20$ ,  $-37 \leq z \leq 37$ . The initial concentrations are  $\gamma_a = 0.667$ ,  $\gamma_b = 0.66$ . The reaction-induced buoyancy number is  $K_\rho = 1.08$ . The wavelength of the CDD cell and the width of the potential well are determined as shown in the inset, they are used to obtain the theoretical curves in figure 13 of Part 1 (Mizev *et al.* 2021).

Below the maximum, a local convective instability arises, which is enclosed inside a potential well. As shown above, the density pocket and conditions for instability development are created under the CDD effect. If this effect is not taken into account, then the liquid in this area remains at rest. That is why this type of instability is called CDD convection (Bratsun *et al.* 2015). The growth of disturbances leads to the development of a spatially periodic convective structure (figure 11,  $t > 2$ ). The integration domain, which corresponds to the width of the experimental cavity, is rather narrow, and therefore only a few cells fit it. However, the numerical simulation with a wider integration domain shows that there exists a periodic system of chemoconvective cells. The obtained pattern is fundamentally different from the usual disordered process of fingering observed commonly in such systems. Most of all, the structure in figure 11 looks like Rayleigh–Bénard convection in a horizontal layer.

An important feature of the system is the independence of the instabilities from each other: they appear in different parts of the medium, are separated by a stably stratified diffusive layer and practically do not interact with each other at the beginning of evolution. Over time, the DLC convection begins to affect the CDD convection by transmitting diffusion signals through the potential barrier separating the two instability zones. Since diffusively coupled instabilities at the beginning have different wavelengths, this causes a LW modulation of one pattern by another. This situation has been studied in detail in Bratsun (2019).

The potential well defining the CDD convection zone slowly expands because of the diffusion of the reactants (compare times  $t = 2$  and  $t = 5$  in figure 11), and the downward motion of heavy salt-enriched cellular structures follows this expansion. This makes it possible to classify this mass transfer regime as a regime under the control of diffusion.



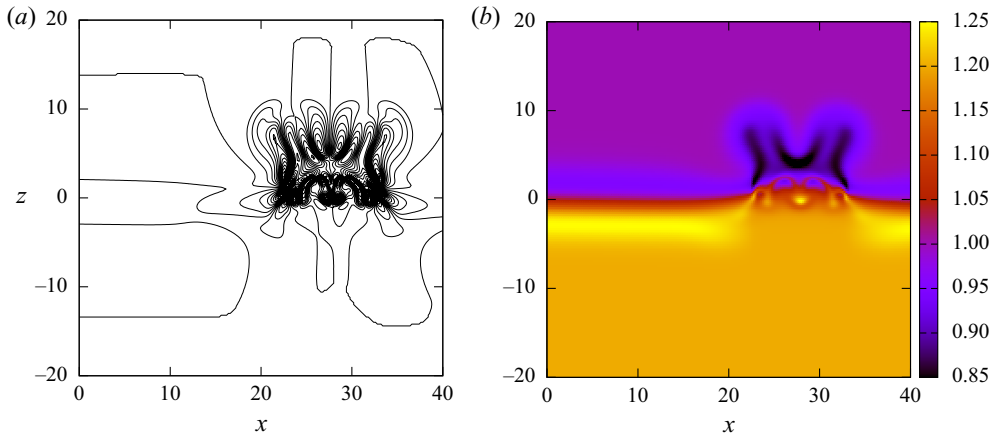


Figure 12. Vorticity field  $\Phi$  (a) and the total density  $\rho$  (b) show the occurrence of a localized convection cell inside a two-layer system when the acid solution enters the system from above in a narrow band defined by  $x = [23, 33]$ . The integration domain is defined by  $0 \leq x \leq 40$ ,  $-20 \leq z \leq 20$ . The initial concentrations are  $\gamma_a = 0.667$ ,  $\gamma_b = 0.66$ . The reaction-induced buoyancy number is  $K_\rho = 1.08$ .

#### 5.4. Convection cell inside two-layer system

The CDD convection gives a great example of how a localized convective structure can be formed in a medium that generates statically stable potential wells of a density field. It is worth noting that self-sustaining convection localized in the bulk of an almost stationary fluid looks very unusual for researchers who have been educated within the paradigm of thermal convection. In the latter case, the medium, as a rule, is heated from the boundary side and convective motion quickly expands to the entire accessible region of the cuvette. The chemical reaction that destabilizes a liquid medium is fundamentally a local tool. By using the CDD instability, we can create, at least in numerical simulation, a convective cell that is statically stable and works autonomously for a sufficiently long time.

To illustrate the above statement, consider a two-layer miscible system placed in a square Hele-Shaw cell (40 per 40 units of dimensionless length), where the lower layer is an aqueous solution of the base, and the upper layer is an aqueous solution of a neutral solute that does not react with alkali. The density of the upper layer is less than the density of the upper. Thus, at the very beginning, the system is stable to perturbations of the RT instability. Suppose that the acid diffuses into the system from above in a narrow band defined by  $x = [23, 33]$ . Then, the reaction occurs only at the intersection of this band and the contact interface. Further, the diffusion of reactants results in the bulk reaction. Figure 12 shows the vorticity contours and total density field at the time  $t = 3$ . One can see that edge effects affect the shape of the reaction front. The CDD instability appears below the potential barrier, while two rising plumes of the DLC convection are developed above the barrier. The vorticity field shows that the fluid motion is localized in a square convective cell measuring 10 by 10 units. The fluid around almost does not take part in the movement.

#### 5.5. Comparison between experimental and theoretical studies

By inspecting the experimental data presented in Part 1 and the theoretical results presented in Part 2, we can conclude that there is a good agreement between experimental observations and theoretical modelling. The principal stability maps

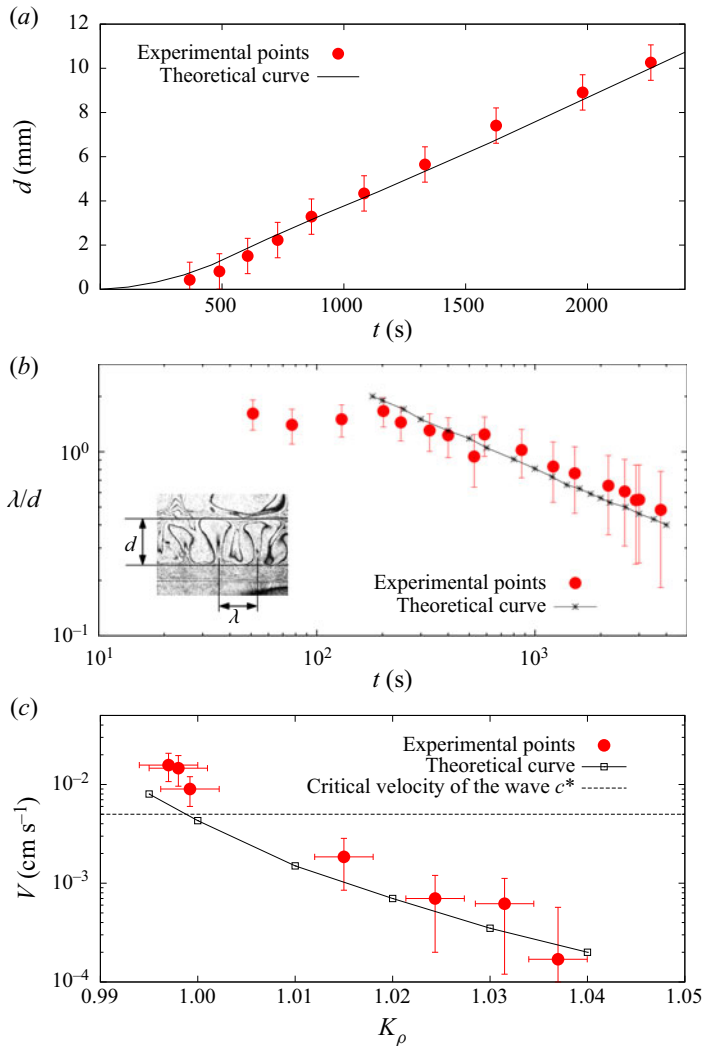


Figure 13. Comparison of experimental data and results of numerical analysis: the growth of the potential well width  $d$  over time (a); the variation of the wavelength of chemoconvective cells  $\lambda$  scaled by the potential well width with time (b); the speed of the reaction front  $V$  in the mode controlled by diffusion ( $K_\rho > 1$ ) and convection ( $K_\rho < 1$ ) (c).

obtained experimentally (see figures 6(b) and 14(a) in Part 1 (Mizev *et al.* 2021)) and theoretically (figure 3) coincide qualitatively and quantitatively. The modes of chemoconvection observed experimentally (see figures 4 and 12 in Part 1 (Mizev *et al.* 2021)), are almost indistinguishable from the regimes obtained in numerical simulation (figures 10 and 11).

Figure 13 demonstrates important quantitative comparisons between experimental data and numerical simulations. Figure 13(a) shows the change in the width of the potential well  $d$  over time. As noted in Part 1 (Mizev *et al.* 2021), the method of Fizeau interferometry makes it possible to qualitatively visualize the spatial distribution of species concentration. This allows comparison with theory. One can see from the figure that, except for the very initial stage, the width of the well increases linearly with time. Good agreement

between theory and experiment indicates that the theoretical reaction–diffusion model works correctly.

Figure 13(b) shows the evolution of the wavelength  $\lambda$  of chemoconvective cells scaled by the potential well width  $d$ . One can see that the cells appear earlier in the experiment than in numerical simulation. This may be due to the fixed amplitude of the perturbations of the streamfunction that we used as the initial state of the system (less than  $10^{-4}$ ) and the slow growth of perturbations at the very beginning of evolution. It is interesting to note that the wavelength of convective cells grows according to the root law  $t^{-1/2}$ , while the width of the potential well, where the cells develop, grows linearly (figure 13a).

The important characteristic of a shock wave is its velocity. The system enters the SW mode only if the wave acquires a speed higher than some critical value  $c^*$ . We have previously shown in Bratsun *et al.* (2017) that the critical velocity can be defined as

$$c^* = \sqrt{Sc} = \sqrt{\frac{\nu}{D_{a0}}}. \quad (5.4)$$

In our problem,  $c^*$  plays the same role as the speed of sound in gas dynamics. This means that, if the density wave moves faster than  $\sqrt{Sc}$ , it behaves as a subsonic analogue of the shock wave in gas. The velocity (5.4) estimated for our problem as  $c^* \approx 17.8$  ( $0.05 \text{ mm s}^{-1}$  in dimensional units) is in perfect agreement with experimental data. We found that, as soon as the propagation velocity of the SW falls below this value, the wave immediately stops and is replaced by a common fingering under the DC mode. Figure 13(c) shows a comparison between the reaction front velocity at the very initial moment of evolution depending on the value of  $K\rho$ . One can notice that the experimental values slightly exceed the velocity values obtained in the numerical analysis. This difference may be related to the value of the Damköhler number, which was fixed in the simulations. Since we do not know the exact value of the reaction rate  $K$  in the medium under consideration, we fixed it to the value  $10^3$ . Most likely, in a real system, this value is a bit higher and the reaction in the experiment proceeds more vigorously.

## 6. Revised and extended classification

It would be interesting and useful to show the new types of instability discussed in this paper in the stability maps of other authors. Figure 14 presents the stability map, which is a modified version of the map proposed in Trevelyan *et al.* (2015). All lines on the figure marked in black have been drawn by the authors of the above-mentioned work. To classify the possible convective instability scenarios, they have analysed the variation of large time asymptotic density profiles as a function of the key parameters of the problem. The main chemoconvection modes are shown in the plane of the governing parameters  $\hat{R}_c$  and  $\delta_c$ . The first parameter is the ratio of the Rayleigh number, which determines the salt buoyancy, to the Rayleigh number of the upper solution. In our notation, it can be either  $R_c/R_a$  (acid at the top) or  $R_c/R_b$  (base at the top). The latter parameter is the ratio of the tabular diffusion coefficients of the salt and the solute dissolved in the upper layer:  $D_{c0}/D_{a0}$  (acid at the top) or  $D_{c0}/D_{b0}$  (base at the top). The stability map is presented for the part of the medium above the reaction front.

The only bifurcation curve we added to the map is marked in red. Let us explain where it comes from. It is first necessary to clarify that the curves  $\hat{R}_c = U_1$  and  $\hat{R}_c = U_2$  correspond to the condition of either the appearance or disappearance of an extremum on the base-state density profile calculated in the limit of large times. More specifically, the curve  $\hat{R}_c = U_1$  is responsible for the occurrence of two extrema at once (one maximum

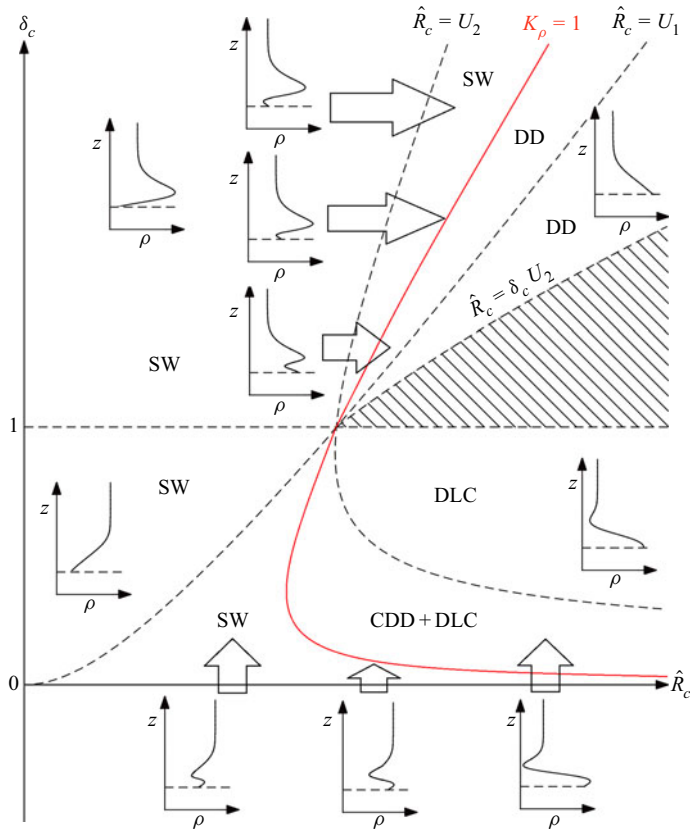


Figure 14. Revised and extended classification based on the analysis of the large time asymptotic base-state density profiles above the reaction front formed in Trevelyan *et al.* (2015). The direction of the reaction front is downwards. The shaded area corresponds to the system at rest. The bifurcation curve of the excitation of the SW mode is marked in red. The map corresponds to the case when, at the very beginning, the system is statically stable. The effect of the CDD is not taken into account.

and one minimum), and the curve  $\hat{R}_c = U_2$  indicates the moment of disappearance of one extremum (either the maximum or the minimum). Thus, we can assume that, in the parametric space between these curves, there are always one maximum and one minimum on the density profile. Therefore, our bifurcation curve  $K_\rho = 1$ , which denotes a balance between the reaction zone density (the local maximum) and the density of the upper layer (the asymptotic density value obtained at  $z \rightarrow \infty$ ), should always be between the curves  $\hat{R}_c = U_1$  and  $\hat{R}_c = U_2$ . Unlike the latter curves,  $K_\rho = 1$  is a true bifurcation curve because it separates the onsets of two qualitatively different flow patterns.

We believe that the analysis of the principal instabilities above the reaction front shown in figure 14 cannot be discussed in isolation from the processes below the reaction front. Therefore, we accept the additional condition that the lower layer is heavier than the upper one:  $\gamma_a R_a < \gamma_b R_b$  (if the acid solution is at the top) and  $\gamma_a R_a > \gamma_b R_b$  (if the base solution is at the top). This condition can easily be satisfied by selecting the initial concentration of the solutions. In this case, the upper and lower layers are separated by a potential barrier. When changing key parameters in the system, one could then observe the types of instabilities shown in figure 14.

Let us discuss the stability map in more detail. Most pairs of reactants considered in the present work satisfy the condition under which the diffusion coefficient of the salt is less than the diffusion coefficient of the solute in the upper layer  $\delta_c < 1$ . The sequence of changes with an increase in salt weight  $\hat{R}_c$  is as follows. If the salt is weightless  $\hat{R}_c \ll 1$ , then a SW mode similar to that shown in [figure 10](#) is observed. In the classification of Trevelyan *et al.* (2015), this type of instability is indicated as RT convection. However, since the lower layer is denser, there exists a SW structure. When we cross the bifurcation curve  $K_\rho = 1$ , the weight of the reaction zone becomes greater than the weight of the upper layer, and the propagation of the SW structure ceases. It is replaced by either the CDD or DLC instability (see [figure 11](#)). Finally, when we cross the curve  $\hat{R}_c = U_2$ , the potential well disappears and only the DLC convection remains in the system at  $\hat{R}_c \gg 1$ .

In the upper part of the stability map  $\delta_c > 1$ , the sequence of events is slightly different: the SW convection also develops first at  $\hat{R}_c \ll 1$ . When we cross the bifurcation curve  $K_\rho = 1$ , the SW is replaced by the DD instability. We found that only the pair of nitric acid and lithium hydroxide falls into this parameter range because their salt satisfies the ratio  $\delta_c > 1$  if the base solution is at the top.

## 7. Final discussion and conclusions

Let us discuss the nature of the new types of instability of heterogeneous reacting media, the characteristic features of which have been discussed above. In our opinion, the fundamental condition for the appearance of these instabilities is the ability of the reaction–diffusion processes to create statically quasi-stable potential barriers. We should note that diffusion alone is not capable of creating such barriers since it is a typical relaxation process that leads to equal concentrations of substances. However, the combined action of the diffusive process and the neutralization reaction, which has a high rate and nonlinear kinetics, can create an inhomogeneous concentration distribution over space and, more importantly, can maintain such a distribution for a sufficiently long time in a quasi-stable state. As is shown above, two potential barriers facing each other form an even more complicated structure, a potential well, which we call figuratively ‘a density pocket’. By cutting the medium with such barriers and pockets, the reaction–diffusion processes create conditions for qualitatively new types of self-organization in a liquid medium.

For example, a SW structure occurs when the density of the reaction zone becomes less than the density of the upper layer ( $K_\rho < 1$ ), and the collapse of the two-layer system begins through the mechanism of the RT instability. In this case, the diffusive layer separating the more dense on top and the less dense on the bottom is unstable to any disturbances. The heavier top layer sinks and the lighter reaction zone floats up, penetrating each other under the gravitational field. When the layers are turned over the physical system searches for a minimum of potential energy trying to find a new equilibrium state. The distinguishing feature of the instability development, however, is that the collapse of the layers does not occur in the entire system, but only in the part separated from the lower layer by the potential barrier. Perturbations propagate exactly to the potential barrier and stop there. Thus, one can observe a SW structure that resembles the phenomenon of a turbulent bore: it has a front separating the region of an immobile fluid (or laminar flow if the observer is in the reference frame of the moving front) and the region of an intensive turbulent flow. This comparison is conditional since a turbulent bore is formed by a surface gravity wave, and we deal with an internal density wave. We should recognize that the potential barrier that limits the development of the RT convection imposes a qualitatively new scenario of the dynamic development of instability, which requires its

separate description in the general classification. The main difference is that the SW structure propagates with an almost flat front, whereas the classical RT instability leads to the development of irregular fingering.

Another example where the reaction–diffusion processes redraw the convective pattern formation scenario is CDD convection ( $K_\rho > 1$ ). In this case, a local potential well arises near the reaction front, the width and depth of which are determined by the effects of CDD, and the quasi-stability of the entire structure is guaranteed by the neutralization reaction. Hypothetically, it could be stated here that the periodic system of chemoconvective cells arising inside such a density pocket is just a strongly deformed DLC convection. Moreover, the region of appearance of the CDD cells in the stability map always adjoins the region where the DLC instability is excited (see [figure 13](#)). However, we believe that this point of view is incorrect because the potential well in the form of a horizontal layer, where the instability develops, imposes completely new properties on convection: periodicity and regularity of the structure. In fact, the cellular structure of the CDD convection most closely resembles the Rayleigh–Bénard convection in a layer with free boundaries, and we use this fact to estimate the local Rayleigh number inside a potential well ([4.21](#)).

In conclusion, we note that the described picture of the phenomena under study is most likely incomplete. The world of even only one neutralization reaction is very diverse: in addition to the strong acids and bases considered in this paper, there are weak reactants; in addition to alkali metal bases, there are more complex organic bases, etc. It is likely that in other, not yet investigated, systems of reacting fluids, the various combinations of potential barriers can significantly change the standard pattern formation in the form of fingering.

**Acknowledgements.** The authors are grateful to V. Pukhnachev, E. Kuznetsov, T. Lyubimova and many other colleagues for a fruitful discussion on the topics.

**Funding.** Authors gratefully acknowledge the support of this work by the Russian Science Foundation Grant No. 19-11-00133.

**Data availability statement.** The data that support the findings of this study are available from the corresponding author upon reasonable request.

**Declaration of interests.** The authors report no conflict of interest.

#### Author ORCIDs.

 D.A. Bratsun <https://orcid.org/0000-0002-3229-2330>;

 A.I. Mizev <https://orcid.org/0000-0001-5233-8271>.

#### REFERENCES

- ALMARCHA, C., TREVELYAN, P.M.J., RIOLFO, L.A., ZALTS, A., EL HASI, C., D'ONOFRIO, A. & DE WIT, A. 2010 Active role of a color indicator in buoyancy-driven instabilities of chemical fronts. *J. Phys. Chem. Lett.* **1** (4), 752–757.
- AVNIR, D. & KAGAN, M.L. 1984 Spatial structures generated by chemical reactions at interfaces. *Nature* **307**, 717–720.
- BEEES, M.A., PONS, A.J., SORENSEN, P.G. & SAGUES, F. 2001 Chemoconvection: a chemically driven hydrodynamic instability. *J. Chem. Phys.* **114**, 1932–1943.
- BRATSUN, D. 2019 Spatial analog of the two-frequency torus breakup in a nonlinear system of reactive miscible fluids. *Phys. Rev. E* **100** (3), 031104.
- BRATSUN, D., KOSTAREV, K., MIZEV, A. & MOSHEVA, E. 2015 Concentration-dependent diffusion instability in reactive miscible fluids. *Phys. Rev. E* **92** (1), 011003.
- BRATSUN, D., MIZEV, A., MOSHEVA, E. & KOSTAREV, K. 2017 Shock-wave-like structures induced by an exothermic neutralization reaction in miscible fluids. *Phys. Rev. E* **96** (5), 053106.
- BRATSUN, D.A. & DE WIT, A. 2004 On Marangoni convective patterns driven by an exothermic chemical reaction in two-layer systems. *Phys. Fluids* **16** (4), 1082–1096.



## Buoyancy-driven flows induced by a neutralization reaction

- BRINKMAN, H.C. 1947 A calculation of the viscous force exerted by a flowing fluid on a dense swarm of particles. *Appl. Sci. Res.* **1**, 27–34.
- CARBALLIDO-LANDEIRA, J., TREVELYAN, P.M.J., ALMARCHA, C. & DE WIT, A. 2013 Mixed-mode instability of a miscible interface due to coupling between Rayleigh–Taylor and double-diffusive convective modes. *Phys. Fluids* **25**, 024107.
- CRANK, J. 1975 *The Mathematics of Diffusion*. Oxford University Press.
- DE WIT, A. 2020 Chemo-hydrodynamic patterns and instabilities. *Annu. Rev. Fluid Mech.* **52** (1), 531–555.
- ECKERT, K., ACKER, M. & SHI, Y. 2004 Chemical pattern formation driven by a neutralization reaction. I: mechanism and basic features. *Phys. Rev. Lett.* **16**, 385–399.
- ECKERT, K. & GRAHN, A. 1999 Plume and finger regimes driven by an exothermic interfacial reaction. *Phys. Rev. Lett.* **82**, 4436–4439.
- FERNANDEZ, J., KUROWSKI, P., PETITJEANS, P. & MEIBURG, E. 2002 Density-driven unstable flows of miscible fluids in a Hele-Shaw cell. *J. Fluid Mech.* **451**, 239–260.
- GÁLFI, L. & RÁCZ, Z. 1988 Properties of the reaction front in an  $A + B \rightarrow C$  type reaction-diffusion process. *Phys. Rev. A* **38**, 3151.
- GANDHI, J. & TREVELYAN, P.M.J. 2014 Onset conditions for a Rayleigh–Taylor instability with step function density profiles. *J. Engng Maths* **86**, 31–48.
- GERSHUNI, G. & ZHUKHOVITSKII, E. 1976 *Convective Stability of Incompressible Fluids*. Keter Publishing House.
- HEJAZI, S. & AZAIEZ, J. 2012 Stability of reactive interfaces in saturated porous media under gravity in the presence of transverse flows. *J. Fluid Mech.* **695**, 439–466.
- HEJAZI, S.H., TREVELYAN, P.M.J., AZAIEZ, J. & DE WIT, A. 2010 Viscous fingering of a miscible reactive  $A + B \rightarrow C$  interface: a linear stability analysis. *J. Fluid Mech.* **652**, 501–528.
- HELE SHAW, H.S. 1898 Investigation of the nature of surface resistance of water and of stream-line motion under certain experimental conditions. *Trans. Inst. Nav. Archit. Lond.* **40**, 21–46.
- HICKERNELL, F.J. & YORTSOS, Y.C. 1986 Linear stability of miscible displacement processes in porous media in the absence of dispersion. *Stud. Appl. Maths* **74**, 93–115.
- KIM, M.C. 2014 Effect of the irreversible  $A + B \rightarrow C$  reaction on the onset and the growth of the buoyancy-driven instability in a porous medium. *Chem. Engng Sci.* **112**, 56–71.
- KIM, M.C. 2019 Effect of the irreversible  $A + B \rightarrow C$  reaction on the onset and the growth of the buoyancy-driven instability in a porous medium: asymptotic, linear, and nonlinear stability analyses. *Phys. Rev. Fluids* **4**, 073901.
- KOZA, Z. & TAITELBAUM, H. 1996 Motion of the reaction front in the  $A + B \rightarrow C$  reaction-diffusion system. *Phys. Rev. E* **54**, 1040R.
- LEMAIGRE, L., BUDRONI, M.A., RIOLFO, L.A., GROSFILS, P. & DE WIT, A. 2013 Asymmetric Rayleigh–Taylor double-diffusive fingers in reactive systems. *Phys. Fluids* **25**, 385–399.
- LOGGIA, D., RAKOTOMALALA, N., SALIN, D. & YORTSOS, Y. 1999 The effect of mobility gradients on viscous instabilities in miscible flows in porous media. *Phys. Fluids* **11** (3), 740–742.
- LOGGIA, D., RAKOTOMALALA, N., SALIN, D. & YORTSOS, Y.C. 1995 Evidence of new instability thresholds in miscible displacements in porous media. *Europhys. Lett.* **32** (8), 633–638.
- LOGGIA, D., SALIN, D. & YORTSOS, Y.C. 1998 A note on the effect of dispersion on the stability of non-monotonic mobility profiles in porous media. *Phys. Fluids* **10** (3), 747–749.
- MANICKAM, O. & HOMSY, G.M. 1993 Stability of miscible displacements in porous media with nonmonotonic viscosity profiles. *Phys. Fluids A* **5** (6), 1356–1367.
- MANICKAM, O. & HOMSY, G.M. 1995 Fingering instabilities in vertical miscible displacement flows in porous media. *J. Fluid Mech.* **288**, 75–102.
- MARTIN, J., RAKOTOMALALA, N. & SALIN, D. 2002 Gravitational instability of miscible fluids in a Hele-Shaw cell. *Phys. Fluids* **14** (2), 902–905.
- MARTIN, J., RAKOTOMALALA, N., TALON, L. & SALIN, D. 2011 Viscous lock-exchange in rectangular channels. *J. Fluid Mech.* **673**, 132–146.
- MIZEV, A.I., MOSHEVA, E.A. & BRATSON, D.A. 2021 Extended classification of the buoyancy-driven flows induced by a neutralization reaction in miscible fluids. Part I. Experimental study. *J. Fluid Mech.* **916**, A22.
- RUYER-QUIL, C.. 2001 Inertial corrections to the Darcy law in a Hele-Shaw cell. *C. R. Acad. Sci. Paris* **329**, 1–6.
- STERN, M.E. 1960 The salt-fountain and thermohaline convection. *Tellus* **12**, 172–175.
- STERN, M.E. & TURNER, J.S. 1969 Salt fingers and convecting layers. *Deep Sea Res. Oceanogr. Abstr.* **16**, 497–511.
- TAN, C.T. & HOMSY, G.M. 1986 Stability of miscible displacements in porous media: rectilinear flow. *Phys. Fluids* **29**, 3549–3556.



- TREVELYAN, P.M.J., ALMARCHA, C. & DE WIT, A. 2011 Buoyancy-driven instabilities of miscible two-layer stratifications in porous media and Hele-Shaw cells. *J. Fluid Mech.* **670**, 38–65.
- TREVELYAN, P.M.J., ALMARCHA, C. & DE WIT, A. 2015 Buoyancy-driven instabilities around miscible  $A + B \rightarrow C$  reaction fronts: a general classification. *Phys. Rev. E* **91** (2), 023001.
- TSUJI, K. & MÜLLER, S.C. 2012 Chemical reaction evolving on a droplet. *J. Phys. Chem. Lett.* **3**, 977–980.
- ZALTS, A., EL HASI, C., RUBIO, D., URENA, A. & D'ONOFRIO, A. 2008 Pattern formation driven by an acid-base neutralization reaction in aqueous media in a gravitational field. *Phys. Rev. E* **77**, 015304.
- ZENG, J., YORTSOS, Y.C. & SALIN, D. 2003 On the Brinkman correction in unidirectional Hele-Shaw flows. *Phys. Fluids* **15** (12), 3829–3836.